CFD Benchmark Tests for Indoor Environmental Problems: Part 3 Numerical Thermal Manikins

Kazuhide Ito*, Kiao Inthavong, Takashi Kurabuchi, Toshikatsu Ueda, Tomoyuki Endo, Toshiaki Omori, Hiroki Ono, Shinsuke Kato, Koji Sakai, Yoshihide Suwa, Hiroshi Matsumoto, Hajime Yoshino, Weirong Zhang and Jiyuan Tu

Interdisciplinary Graduate School of Engineering Science, Kyushu University, 6-1 Kasuga-koen, Kasuga, Fukuoka, 816-8580 Japan

Abstract: Recent indoor environmental design is requested to create comfortable and safety space in addition to the maximizing the energy conservation performance in buildings. In this point of view, it is important to enhance the prediction accuracy of indoor environmental quality in design stage. Commercial Computational Fluid Dynamics (CFD) software is practically applied in indoor environmental design recent years but the prediction accuracy of CFD simulation depends on the understanding for the fundamentals of fluid dynamics and the setting of appropriate boundary and numerical conditions as well. The series of this study aimed to provide with the practical information such as prediction accuracy and problematic areas related to CFD applications in indoor environment, air conditioning and ventilation, and then performed benchmark tests and reported the results. Especially in this Part 3, benchmark test results for numerical thermal manikins were introduced. SST k-ω model with fine mesh could provide sufficient accurate results and showed good agreement with experimental results.

Keywords: Indoor environment, Computational Fluid Dynamics, Benchmark test, Numerical thermal manikin.

1. INTRODUCTION

CFD has become practical design tool for creating indoor environment of good quality and performance, and is absolutely imperative in recent years. The prediction accuracy of CFD simulation depends on the understanding for the fundamentals of fluid dynamics and the setting of appropriate boundary and numerical conditions as well and hence the organization and maintenance of the database concerning benchmark test associated with applying CFD to indoor environmental problems is important.

The overarching objective of this research project is to compile benchmark test results of CFD that relate to indoor environmental problem. Though various types of flow fields are found in indoor environment, we have classified those flow fields into eight categories based on literature review: (1) Isothermal 2-D/3-D airflows, (2) Non-isothermal 2-D/3-D airflows, (3) Cross-ventilation airflows, (4) Floor heating (panel) systems, (5) Numerical thermal manikins, (6) Air-conditioning airflows, (7) Residential kitchen airflows, (8) Fire-induced flow. Concerning the benchmark test results for targeting (1) Isothermal 2-D/3-D airflows and (2) Non-isothermal 2-D/3-D airflows, (3) Cross-ventilation airflows, (4) Floor heating (panel) systems, the details have been discussed in previous reported paper of this research series (Part 1 Benchmark test for isothermal/non-isothermal flow in 2D and 3D room model [1], and Part 2 Benchmark test for Cross-ventilation airflows and Floor heating systems [2]. In this paper, benchmark test results for (5) Numerical thermal manikins, were introduced and discussed.

It is common knowledge that human bodies have varied perceptions of thermal comfort and sensations depending on indoor environmental factors and also heating and cooling systems. Environmental factors related to human thermal sensation are known as air temperature, radiative temperature, air velocity, and air humidity. Since humans can tolerate only a limited range of internal (core) temperatures, comfort is said to correlate with the amount of sensible and latent heat released by the human body.

Thermal manikins are widely used to evaluate indoor environments in buildings and cars with respect to human thermal sensation in field measurement and/or climate chamber experiments [3]. Thermal manikins have also been widely used as models to study indoor environments by running intrinsic numerical simulations of airflows in heated and cooled spaces. It is true that various unavoidable errors occur in numerical simulations because of factors such as modeling, numerical algorithms, and models of turbulent flow. This is why simulation results must be validated by comparisons with experimental results under clear and well-defined boundary conditions.

*Address correspondence to this author at the Interdisciplinary Graduate School of Engineering Science, Kyushu University, 6-1 Kasuga-koen, Kasuga, Fukuoka, 816-8580 Japan; Tel: +81 92 583 7628; Fax: +81 92 583 7627; Email: ito@kyudai.jp

E-ISSN: 2409-9821/15

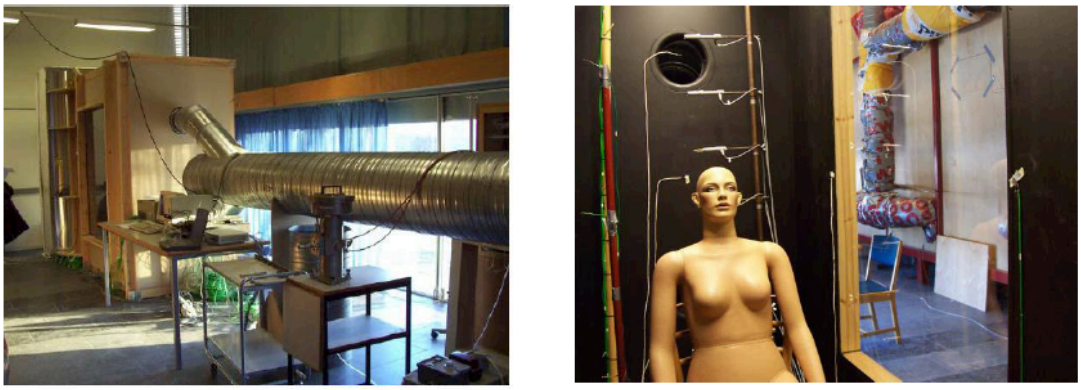

(a) Chamber exterior (b) Thermal manikin inside the chamber

Figure 1: Scene of the experiment.

A number of studies have been published [4] that contain experimental data on thermal manikins. Such data were specifically intended to be used to validate simulation results, with one published by Martinho *et al.*, [5].

2. BENCHMARK TESTS ON A NUMERICAL THERMAL MANIKIN

We perform validation tests on three cases by comparing experimental data with the results from numerical simulations involving thermal manikins. The three scenarios are;

(1) a thermal manikin on a chair in direct contact with countercurrent airflow in a chamber with indoor airflows simulated,

(2) a thermal manikin in a chamber with displacement ventilation, and

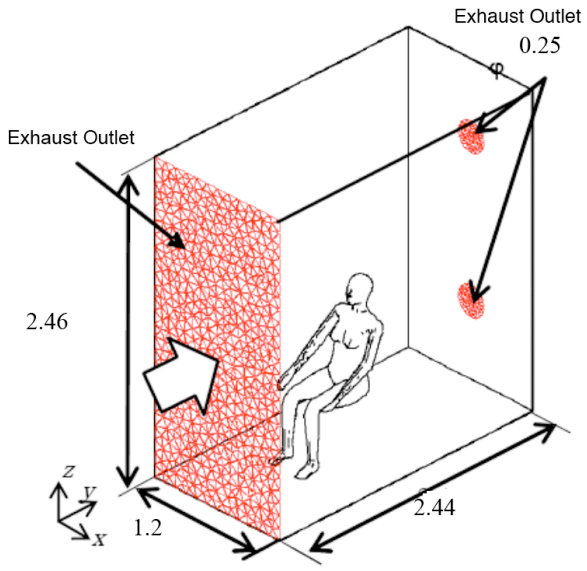

Figure 2: Schematic of experiment equipment.

(3) a thermal manikin in a wind tunnel with relatively strong wind condition.

2.1. Thermal Manikin on a Chair in Direct Contact with Countercurrent Airflow in a Climate Chamber

2.1.1. Experiment Outline

This experiment was conducted at Aalborg University in Denmark [6]. Photos of the experimental equipment and its schematic are shown in and Figures **1** and **2**, respectively. Exhaust outlets were placed 0.6 m away from the ceiling and 0.6 m away from the floor on the rear wall of the cuboid (rectangular parallelepiped) climate chamber. The chamber dimensions were: width = 1.2 m, depth = 2.44 m, height = 2.46 m. Exhaust outlets were connected *via* ducts to exhaust fans. In the experiments, a uniform airflow entered the front inflow area at 20.4°C and a speed of 0.27 m/s. The chamber was made from 12-mm plywood, the thermal conductivity (rate of heat transfer) was 0.15 W/m/K, and the outside thermal conductivity was 10 W/m/K. The thermal manikin was placed naked at x = 0.6 m (central) and y = 1.22 m (hip center); the surface temperature of the manikin was kept constant at 34°C. The thermal manikin represents the Figure of a woman, with its surface partitioned into 17 parts.

Surface temperatures were measured at given points in the chamber; distributions of temperature and speed were also measured at the points L1 to L4 shown in Figure **3**. Figure **4** shows the vertical distribution of inflow temperatures. The measurements included heat discharged at the points where the thermal manikin was placed. The measured data were published as an Excel spreadsheet *via* online on www.cfd-benchmarks.com.

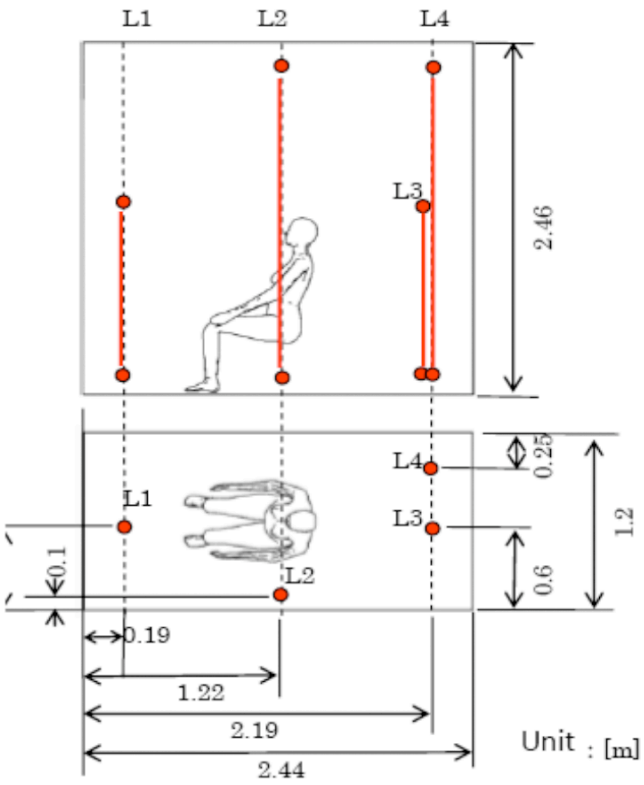

Figure 3: Locations for line measurements of temperature and airflow speeds.

2.1.2. Analysis Outline

Table **1** summarises the boundary conditions used with commercial CFD software, IDAJ/STAR-CD (referred to as Code D from here on). The MARS difference scheme and SIMPLE pressure-velocity coupling was used. The solver combined the Monte Carlo method and the Zone method for radiative analysis [7]. Four turbulence models were evaluated: SST k-ω; realizable k–ε; low-Re k–ε; and v2-f models. Code D contains an equation (ε and k) for terms related to the turbulence kinetic energy P_B that is produced by buoyancy. The coefficient for the buoyant force-generated turbulence kinetic energy in the ε equation is $c_{\varepsilon 3}$ = 1.44 (P_B > 0), with all other terms set to zero [2].

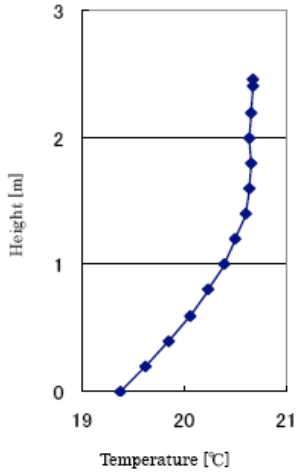

Figure 4: Vertical distributions of inflow temperatures.

To determine mesh dependence, two types of grid design, standard mesh (Mesh1) and a fine mesh (Mesh2, this mesh was further refined for the manikin surface) were prepared. Tables **2**, **3** and Figure **5** show the mesh design. The thickness of the wall-surface first cell was 0.5 mm for the manikin surface and 1 mm for the chamber. We used an enlargement rate of 1.1 and

Table 1: Boundary Conditions

Fluid Calculation	Inflow/outflow Outlets		Inflow Outlets	Outflow Outlet
	Inflow/ Outflow Boundary Conditions	Speed	0.27 m/s	Pressure Boundaries
		Temperature	Figure 3	
		Turbulence Intensity	0.05	
		Turbulence Length	0.16 m	
	Wall Boundary Conditions	Speed	no-slip	
		Temperature	The temperature being sought through using radiative calculation routine	
Radiation Calculation		Solid Surface	Human Model	Wall body
		Temperature	34 ˚C	Heat resistance from the inside wall to the outdoor air: 0.18 m^2 K/W Outdoor air temp. 20.4 ˚C
		Emissivity [-]	0.9	0.9
		Convective Heat Flux	The temperature being sought through using radiative calculation routine	

Table 2: Details of Grid Design

Mesh	Object for Test	Region	Cell Width mm	Surface Cell No.	Spatial Cell No.
mesh1 (Std. Mesh)	Human Body	Face/Hands	5–20	9,304	300,496
		Feet	30		
		Other	35		
	Chamber	Exhaust Outlet	50	9,696	
		Around Feet	30		
		Other	100		
			(Total)	19,000	
mesh2 (Fine Mesh)	Human Body	Face/Hands	3–10	58,264	1,219,813
		Other	10		
	Chamber	Exhaust Outlet	50	18,138	
		Around Feet	10		
		Other	100		
			(Total)	76,402	

Table 3: Mesh Parameters

Test Subject	Thickness of the 1rst Mesh from the surface mm	Enlarge ment ratio	No. of Layers
Human Body	0.5	1.1	5
Chamber	1	1.1	5

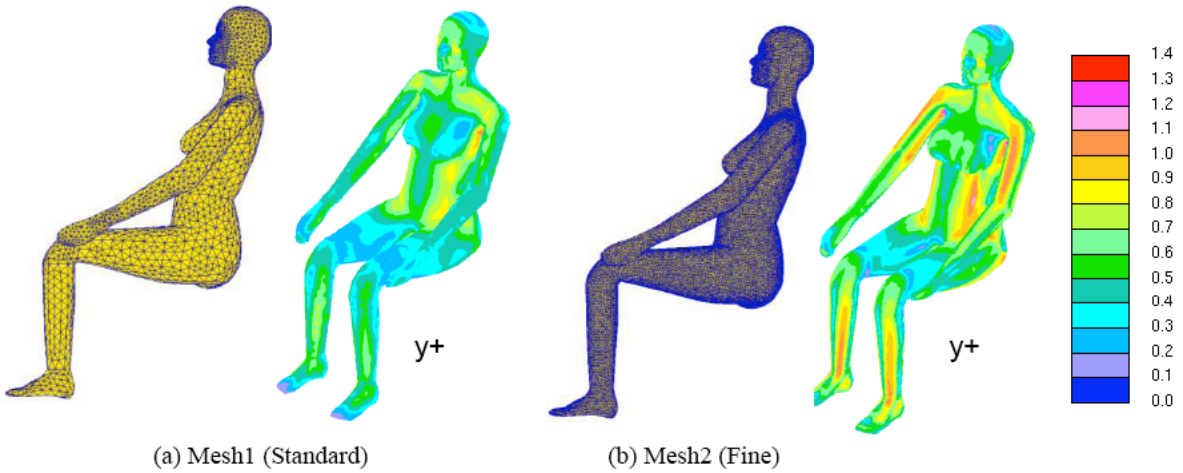

Figure 5: Distribution of y+ values and state of manikin surface partitions.

created a five-layer boundary-layer mesh. The value of *y*+ (wall unit) for the wall-surface first cell is a little larger in the standard model than in the fine mesh.

Results for the wind speed distribution in a top (horizontal) cross-sectional view –, are shown in Figure **6**. The airflow branches out from the lower area after colliding with the front surface of the lower legs. The speed of the airflow after branching into different directions was faster in Mesh2 than in Mesh1. The manikin surface mesh resolution for Mesh2 was high, and on the basis of this resolution we were able to determine the velocity. For Mesh1, the air velocity was averaged owing to the larger mesh elements. Since the thickness of the cell was maintained at 0.5 mm, the value for y^+ in Mesh2 increased. The SST k-ω model was used in analyses for Mesh1; all other turbulence models were used for analyses for Mesh2.

2.1.3. Analysis Results

Figure **7** shows the distributions of velocity magnitude, turbulence kinetic energy *k*, and dissipation

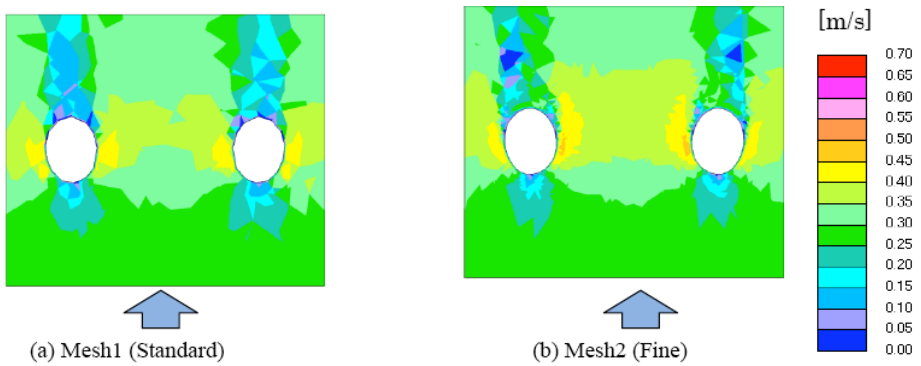

Figure 6: Wind speed distributions at top (horizontal) cross sections. The hollow circles are the two legs of the manikin. The arrow represents the flow direction.

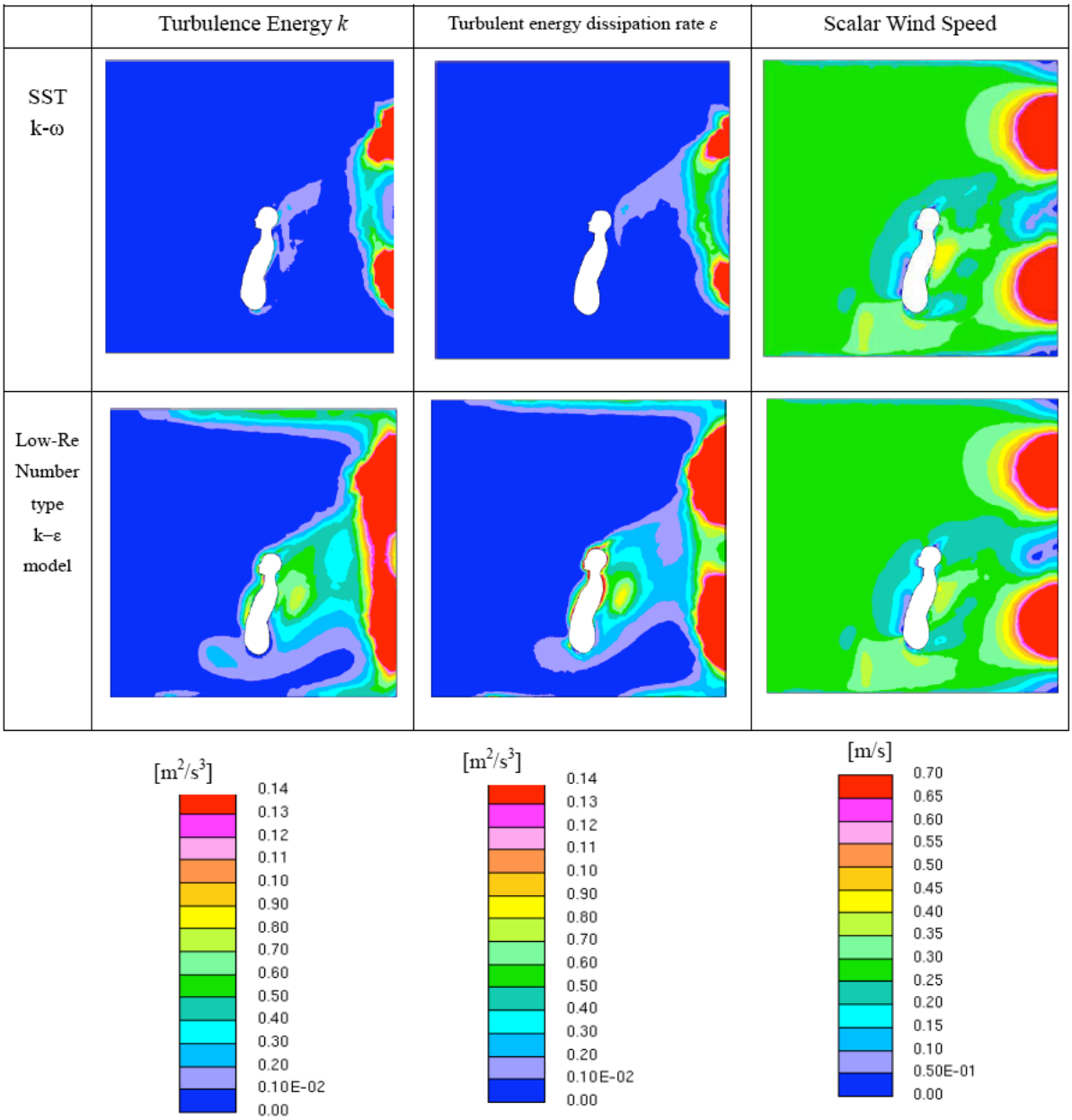

Figure 7: Distributions of scalar wind speed, turbulence energy *k*, and the turbulent energy dissipation rate *ε* from two turbulence models.

rate of turbulence kinetic energy ε in the vertical midplane cross section that includes the manikin. These results are for the SST k- ω turbulence model and the low-Re k–ε turbulence model. Although the velocity distributions are nearly the same for both models, values for k and ε from the SST k-ω model are less than those from the low-Re k–ε model. Because k and ε for the low-Re k–ε model were overestimated, differences occurred between the two models.

Figure **8** compares predicted and measured values for turbulence kinetic energy along line L3 which is behind the manikin. The Figure shows little difference in results between Mesh1 and Mesh2 for the SST k-ω turbulence model. Calculated values for the SST k-ω and v2f turbulence models matched very closely. Although the calculated values from the realizable k–ε turbulence model at a height of both 0.275 m and 0.55 m were similar to the experimental data, this model significantly overestimated the turbulence kinetic energies at heights at and above 0.875 m. The values produced by the low-Re turbulence model were overestimated.

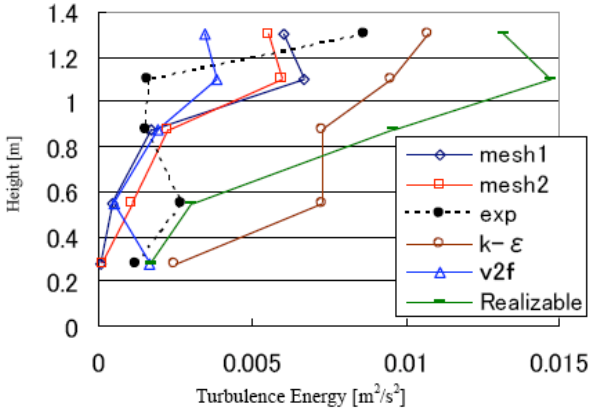

Figure 8: Calculated and measured turbulence kinetic energies.

Figure **9** shows measured and calculated values of velocity at positions L1 and L3. There were almost no significant differences between Mesh1 and Mesh2 when the SST k-ω turbulence model was used. Differences among turbulence models were also small. In addition, the calculated values matched measured values.

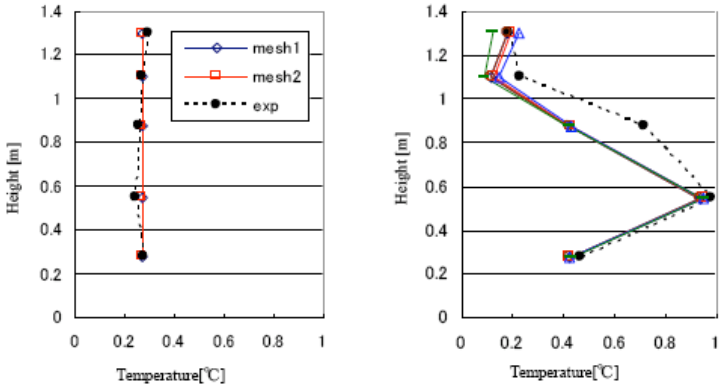

Figure 9: Calculated and measured values for scalar wind speed.

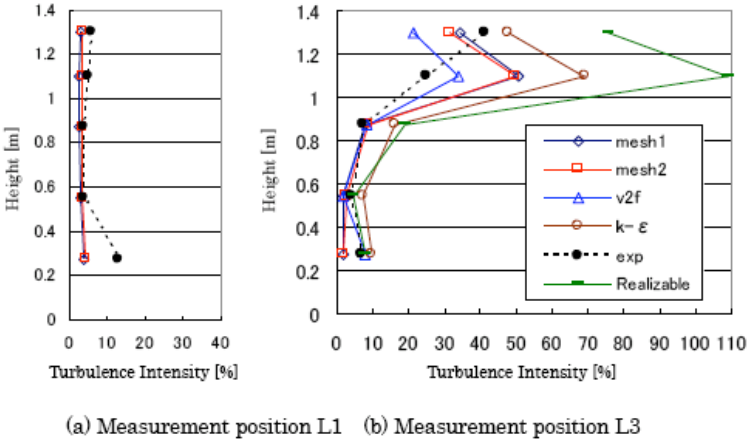

Figure 10: Calculated and measured values for turbulence.

Figure **10** compares measured and calculated values for the turbulence intensity at points L1 and L3. Turbulence intensity *I* was obtained by dividing the RMS velocity fluctuation by the average velocity *U*. The Figure shows almost no significant differences between Mesh1 and Mesh2 when the SST k-ω turbulence model was used. Calculated values generally matched measured values. Among the turbulence models used at position L3, the v2f model most closely agrees with measured values. Results from the SST k-ω turbulence model are too large at the height of 1.1 m; however, if this single point is ignored, the Figure shows generally good agreement between the SST k-ω model and experiment. For heights above 0.875 m, the low-Re and realizable k–ε turbulence models both produced intensities that were too large compared with that of the experiment.

Figure **11** shows measured and calculated values for air temperatures at positions L2 and L4 for simulations in which the SST turbulence model was used. Almost no differences occurred between Mesh1 and Mesh2, and both agree with experimental values. Results from simulations using the other turbulence models generally agree with those shown for the SST k-ω turbulence model. Measured and calculated values for surface temperatures in the chamber are shown in Figure **12**. Generally there is good agreement. At point 31, which represents the area around the feet of the manikin, the temperature rose due to heat given off by the manikin. Also included in the Figure are calculated values for situations in which we slightly changed the measurement position from 31 to 31' and to 31'' (see Figure **12**).

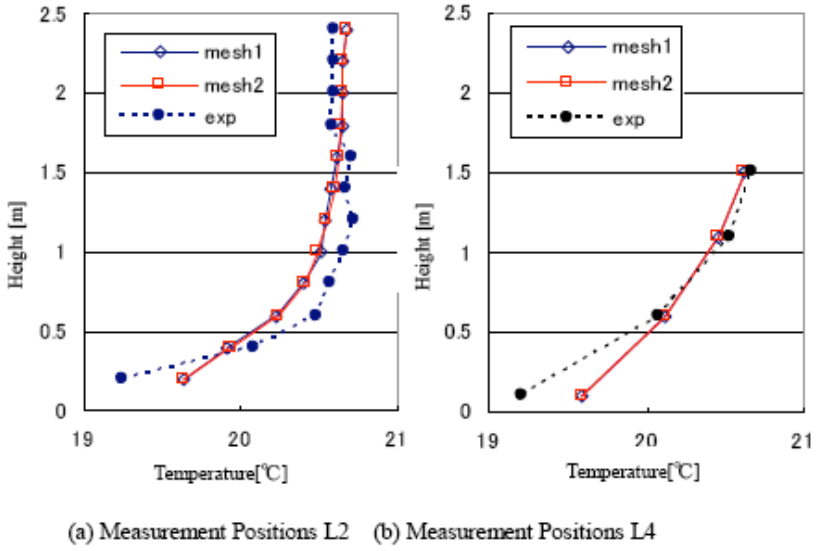

(a) Measurement Positions L2 (b) Measurement Positions L4

Figure 11: Calculated and measured air temperatures.

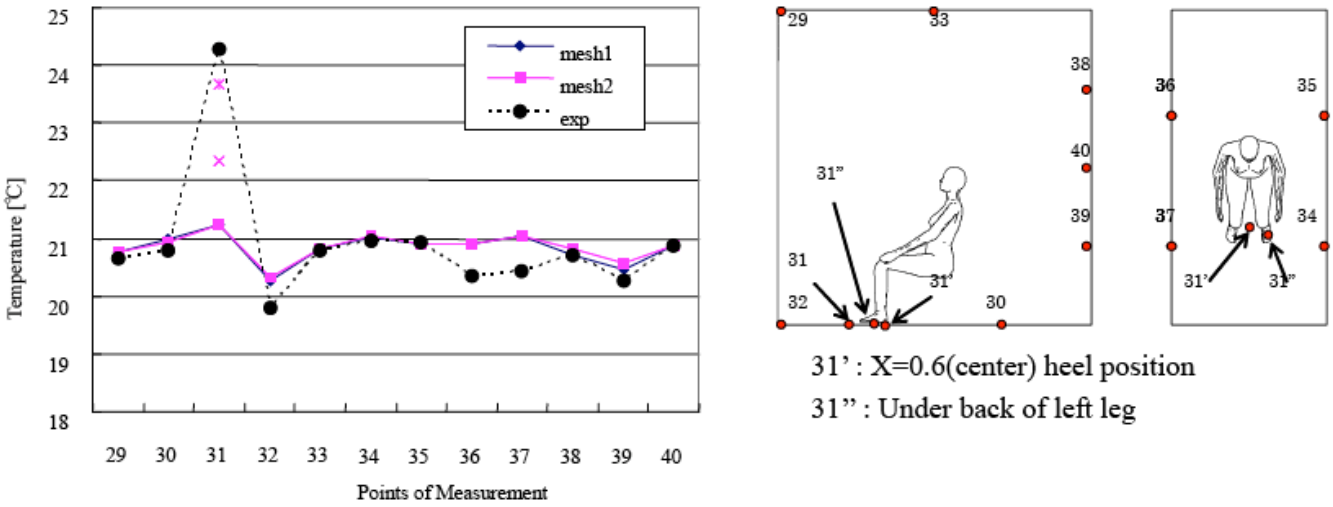

Figure 12: Calculated and measured values for air temperatures on chamber surfaces.

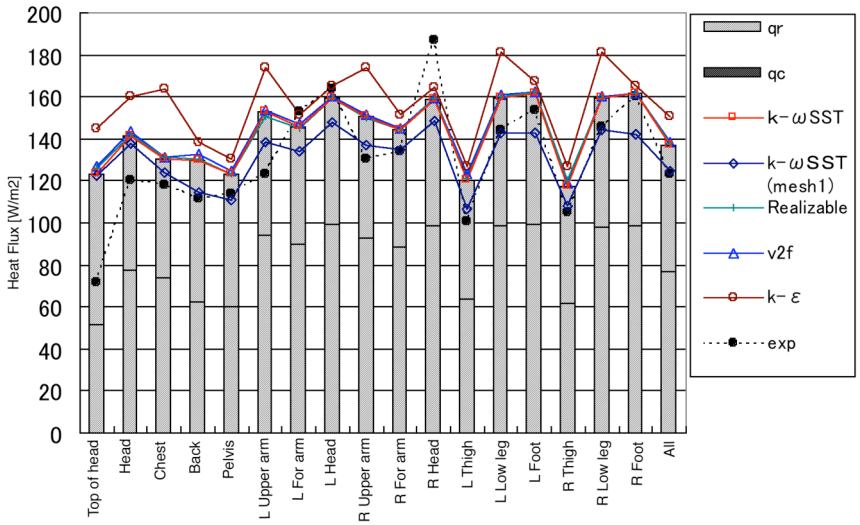

Figure 13: Calculated heat fluxes for each body region from different turbulence models.

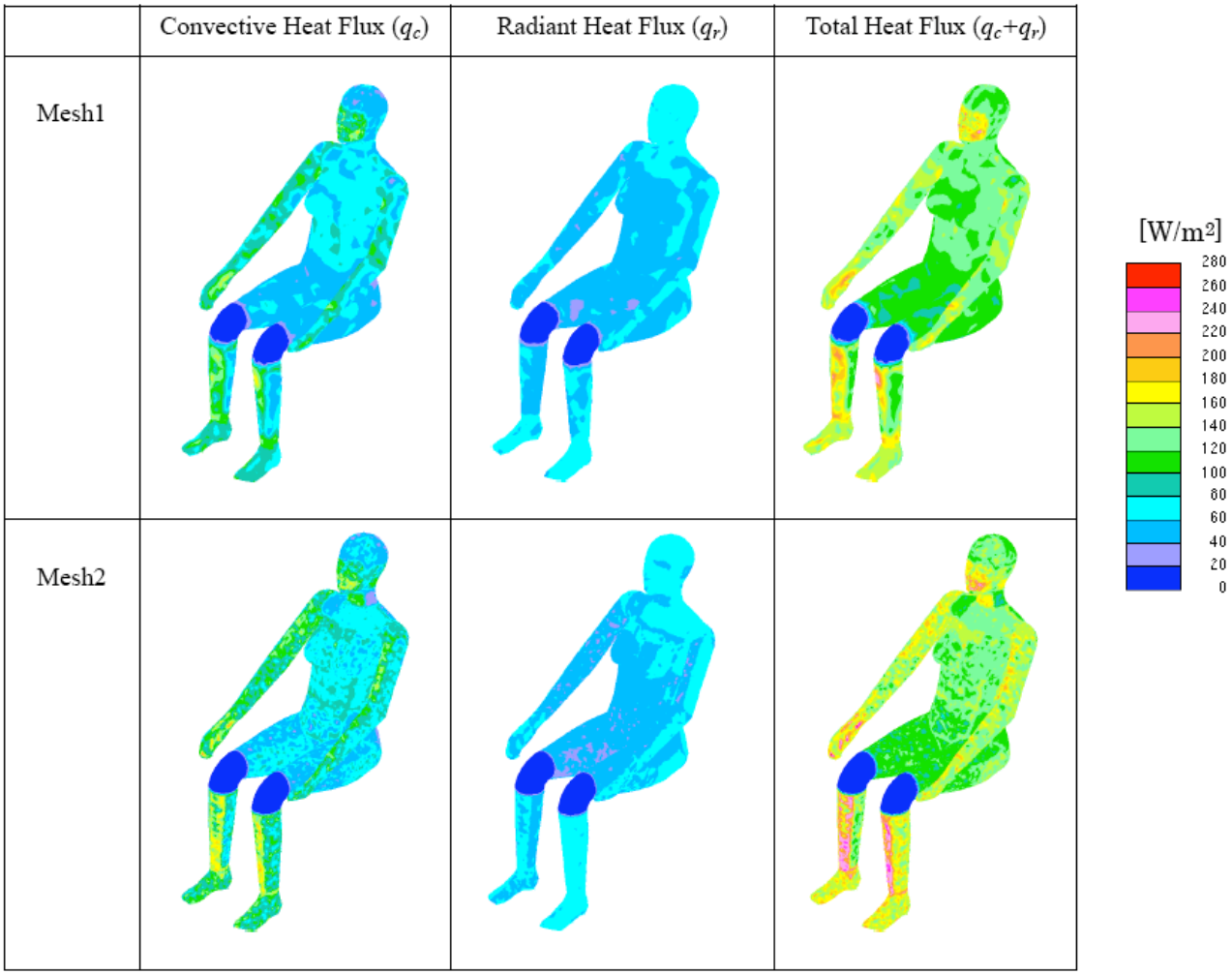

Figure 14: Calculated heat flux distributions on manikin surfaces using SST k-ω turbulence model.

Figure **13** compares measured and simulation results for heat flux from the 17 body segments of the manikin. The heat flux is contributed by radiative heat flux given by q_r flux and convective heat flux, *qc*; where the contributions are shown as bar in Figure **13** for the SST k-ω turbulence model only. Results for the SST k-

ω (Mesh2), realizable, and v2f all corresponded well. With the exception of the top area near the head, these simulation results were roughly 5–20 W/m^2 larger than measured values. Convective heat fluxes for all body regions were overestimated for the low-Re k–ε turbulence model.

Values for convective heat flux from simulations that used Mesh1 were larger in each body region compared with results using Mesh2. Figure **14** shows distributions of heat flux over manikin surfaces from the SST k-ω turbulence model. Calculated convective heat flux for Mesh2 was larger than in Mesh1 for airflows that impinged on the following regions: lower legs, upper legs, front chest, each front surface for the hands, and the area around the mouth. No large differences in radiative heat flux were seen between the mesh models. Differences in total heat flux result from differences in convective heat flux.

2.1.4. Discussions

Prism mesh layers were applied onto the skin (solid) surface of the manikin to allow boundary-layer cells. Here, the height of the first cell was set to 0.5 mm. Then we compared the second cell with the first at an extrusion layer enlargement ratio of 1.1 and created a five-layer extrusion. To test the choice of an enlargement ratio of 1.1, simulations were performed where the extrusion layer enlargement ratio was set to 1.05 and to 1.20. As shown in Figure **15**, effects of the mesh design on the total heat flux were small.

Martinho *et al*., [5] used this same method and reported benchmark test results using the SST k-ω and standard k–ε turbulence models. The number of mesh elements for the manikin was 95,000, and the spatial domain 1,400,000. Their results showed that air velocity profiles along L3 were almost identical for both

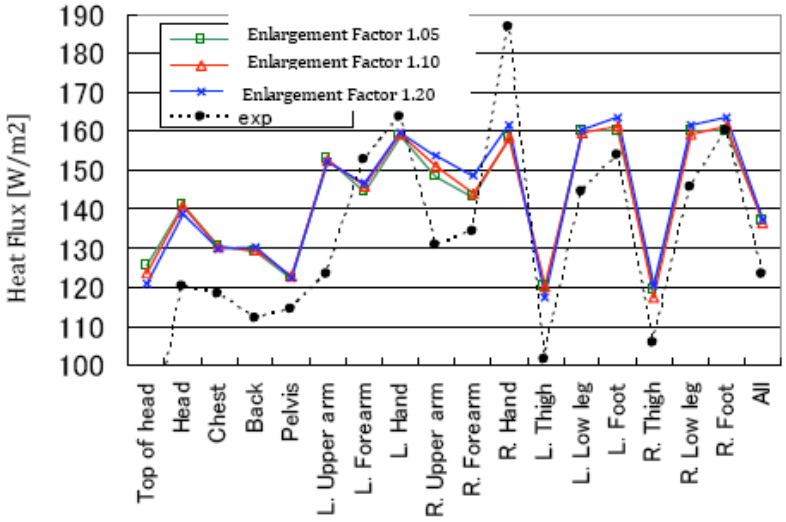

Figure 15: Effects of enlargement factor for manikin extrusion layers on computed manikin heat fluxes at selected body regions.

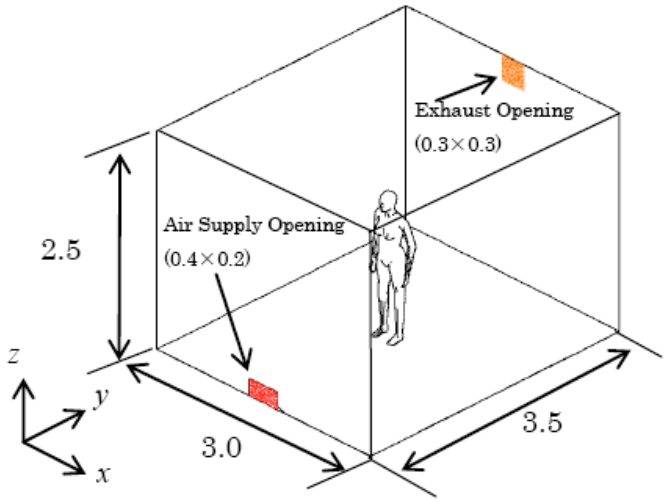

Figure 16: Schematic of experimental ventilation chamber.

turbulence models but the turbulence intensity for the standard k–ε turbulence model was overestimated. However, values of turbulence intensity from the SST turbulence model almost matched measured values. Their results agree with the results in this study.

Martinho *et al*., [5]'s heat flux results on surfaces of the manikin from the SST k-ω turbulence model were about 0–20 W/m^2 higher (depending on location) than measured values. Although these results closely match our results, they were much closer to the measured values for the head, back, and abdomen. Their simulation results using the standard k–ε turbulence model were lower than measured values; values of heat flux for the feet, lower legs, hands, and front chest were particularly underestimated. In this study, the overall heat flux was overestimated when the low-Re k–ε was used, showing trends completely opposite to those found by Martinho *et al*. [5]. In their analysis, the value of y^+ was less than five for the first cell of the manikin which is too small for the standard k–ε turbulence model. Martinho *et al*. [5] did not mention whether or not they switched to hybrid functions to handle low-Re or high-Re in accordance with fluctuating y^+ values.

In this section, CFD simulations of a numerical manikin in a countercurrent flow were simulated, and compared with experimental results. The turbulence kinetic energy in the region behind the manikin obtained from the SST k-ω and v2f turbulence models agreed fairly well with experimental data; however, this was over-predicted by the realizable and low-Re models. All turbulence models produced air velocity and temperature distributions well with measured values. Although simulation results were relatively larger than measured results for the heat flux from manikin surfaces, they generally agreed for the most part. Values of heat flux from the low-Re k–ε model were high compared with experiment. For simulations using the SST k-ω turbulence model, the standard computational mesh generally produced smaller values for the heat flux than those obtained with the fine mesh.

2.2. Thermal Manikin in a Chamber with Displacement Ventilation

CFD benchmark tests were performed against the Displacement Ventilation Case published in the section on the numerical thermal manikin (CSP: Computer Simulated Person) of the CFD benchmarks.

2.2.1. Experimental Setup

This experiment was conducted in the Institute of Industrial Science at the University of Tokyo. Figure **16** shows the schematic of the experimental chamber and thermal manikin used in the measurement. An air supply opening (0.4 × 0.2 m) was placed at the bottom of the rectangular chamber (width = 3.0 m, depth = 3.5 m, height = 2.5 m). A uniform airflow entered the chamber at 21.8°C and with velocity of 0.182 m/s. Air

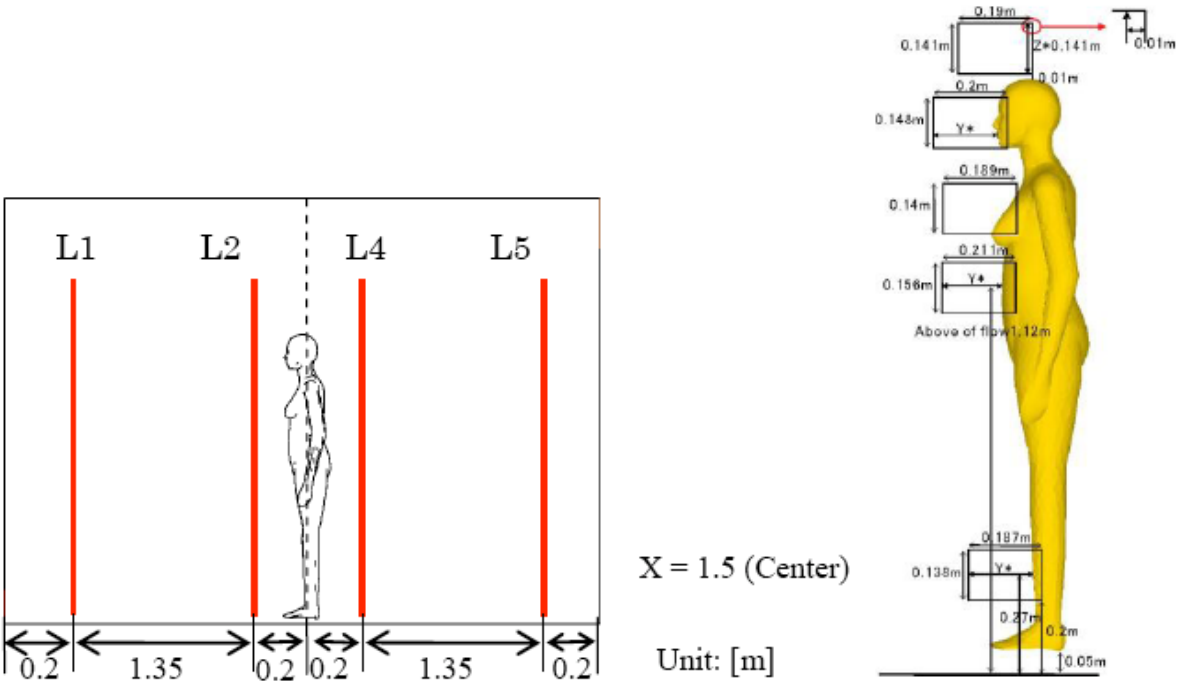

Figure 17: Measurement positions for temperature and airflow speed distributions.

exited the chamber through a 0.3 m × 0.3 m exhaust outlet that was located on the rear wall under the ceiling. The thermal manikin was placed at x = 1.5 m (center) and y = 1.75 m (center of head). The total heat generated from the thermal manikin was kept constant at 76 W (the heat flux remained constant at 51.6 W/m^2 for each region). Temperature and air velocity distributions were measured along lines L1 to L5 shown in Figure **17**. In addition, particle image velocimetry (PIV) was used to take detailed measurements in the following regions: areas around lower legs, chest, lips, and top of head. The temperature was measured at each point on the thermal manikin [8].

2.2.2. Analysis Outline

The following boundary conditions were used:

- Inflow boundary: temperature = 21.8°C; airflow speed = 0.182 m/s; turbulence intensity = 0.3; Turbulence flow length scale = 0.1-m;
- Outflow boundary: pressure boundaries;
- Wall-surface heat transfer: heat insulation;
- Heat fluxes for manikin: 51.6 W/m^2; emissivity: 0.9 for both the manikin and wall body;

The numerical setup included: turbulence model was the SST k-ω model as the baseline, and for comparison we also tested the low-Re k–ε, realizable k–ε, v2f, and high-Re k–ε; discretization scheme was MARS; pressure-velocity coupling was SIMPLE; and radiation analysis: CalcRad (Monte Carlo method + Zone method [7]).

To confirm mesh independence, we performed simulations using three mesh designs, detailed in Table **4** and Figure **18**. Mesh0 was a coarse mesh that had 4,130 elements for the manikin surface, about 20,000 elements for the chamber walls, and 450,000 elements for the fluid domain. Mesh1 was a normal mesh with 6,080 elements (about 1.5 times Mesh0) for

Table 4: Detail Information of Grid Design Around Human Body

Mesh	Object for Test	Region	Cell Width mm	Surface Cell No.	Spatial Cell No.
Mesh2 (Fine Mesh)	Human Body	Face/Hands	3–10	57,654	1,443,153 (Cases where there are 10 extrusion layers in human body) [1,697,775]
		Other	10		
	Chamber	Exhaust Outlet	50	26,026	
		Around the feet	10		
		Other	100		
			(Total)	83,680	
Mesh1 (Normal Mesh)	Human Body	Face/Hands	5–20	6,080	497,745
		Feet	30		
		Other	35		
	Chamber	Exhaust Outlet	50	20,616	
		Around the feet	30		
		Other	100		
			(Total)	26,696	
Mesh 0 (Coarse Mesh)	Human Body	Face/Hands	15–50	4,130	451,896
		Other	50		
	Chamber	Exhaust Outlet	50	19,986	
		Around the feet	50		
		Other	100		
			(Total)	24,116	

Boundary Layer Mesh (Extrusion Conditions from the Solid Surface)

Object for Test	Thickness of first mesh from surface (mm)	Enlargement Factor	No. of Layers
Human Body	0.5	1.1	5
Chamber	1	1.1	5

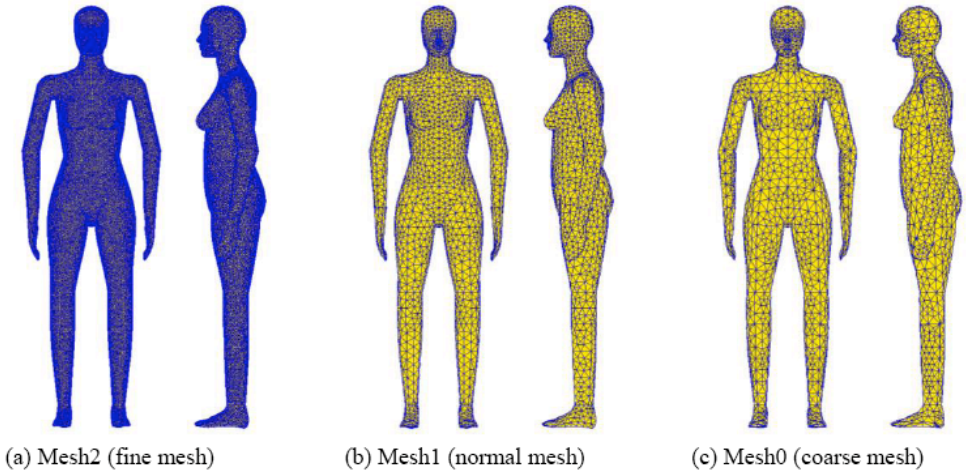

Figure 18: Surface mesh design of numerical thermal manikin.

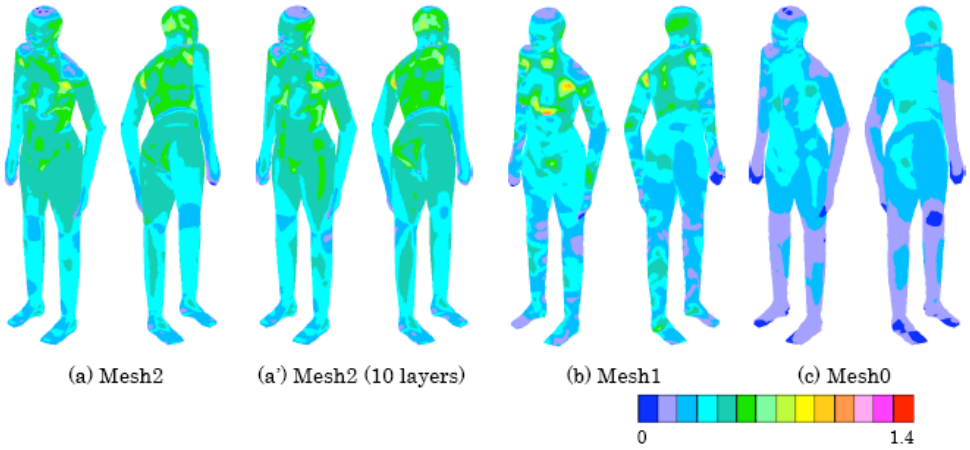

Figure 19: Distributions of *y*+ values on manikin surfaces.

the manikin surface. Mesh2 was a fine mesh with 57,654 elements (more than 10 times Mesh0) for the manikin surface and about 1,400,000 elements for the fluid domain. The thickness of the first cell of the boundary-layer mesh was 0.5 mm for the manikin surface and 1 mm for the chamber. The enlargement factor was set to 1.1, and the number of layers was set to five. We also included a calculation in which we used ten layers for Mesh2. The value of y^+ over the manikin surface was less than one for all meshes, as shown in Figure **19**.

2.2.3. Analysis Results

Figure **20** compares measured and calculated values for the turbulence intensity. At line L1 near the supply opening, the measured turbulence intensity was about 50%, while the calculated values were almost zero excluding the areas around the floor and ceiling. The measured turbulence intensity at point L2 (right in front of the manikin) was about 50%, but calculated values vary with height, and several differences occur for different mesh models. At line L4 (behind the manikin), calculated values at height = 1 m were significantly smaller than the measured value. At line L5 (right in front of the exhaust outlet), calculated values for Mesh0 and Mesh1 were almost the same; however, these values were still lower than the measured value. The value calculated from Mesh2 at L5 was too large at height = 1.4 m.

Figure **21** shows air velocity distributions from simulations and experiment. At positions L1, L2, and L5, calculated air velocity distributions were in good agreement with measured values. At position L4, all calculated values at height = 1 m exceeded the measured values, but all other calculated values at L4 agreed with experiment.

Figure **22** shows distributions of vertical velocity components around the front surface of the manikin. In the plots, the x-axis shows horizontal distances from the manikin surface. With the exception of the top of the head, air velocities for all other body regions

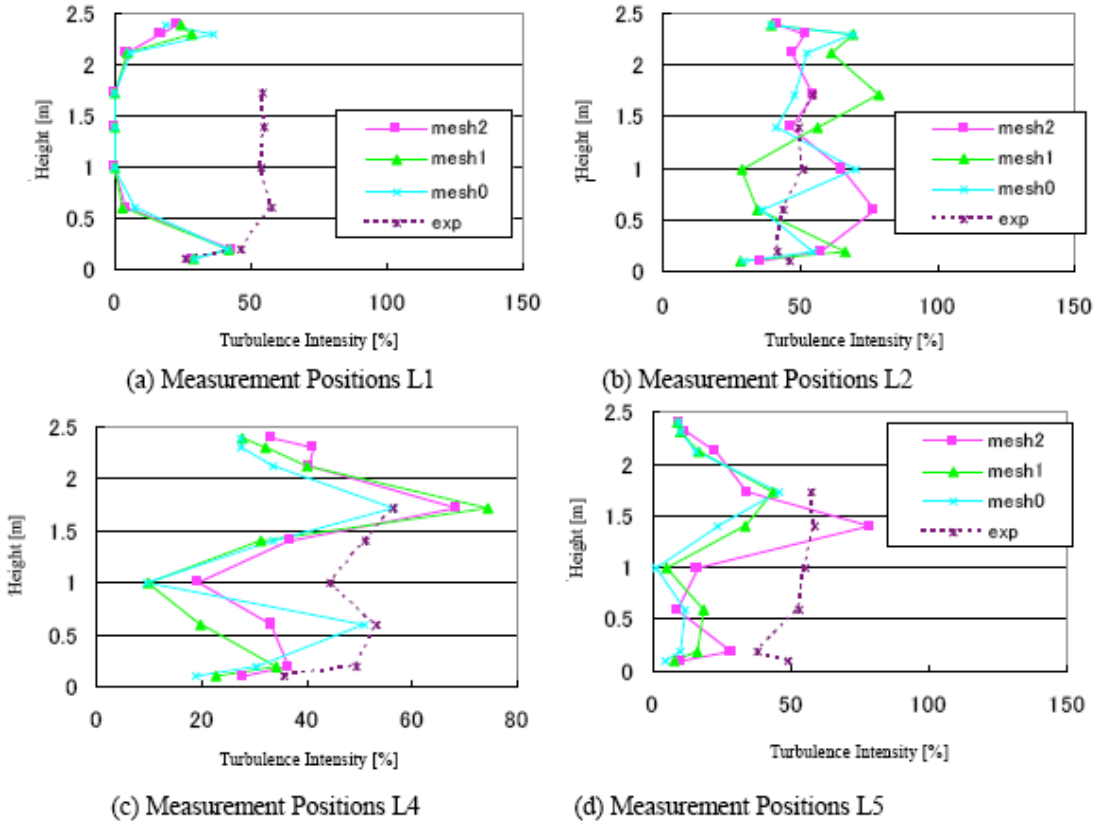

Figure 20: Calculated and measured distributions of turbulence intensity.

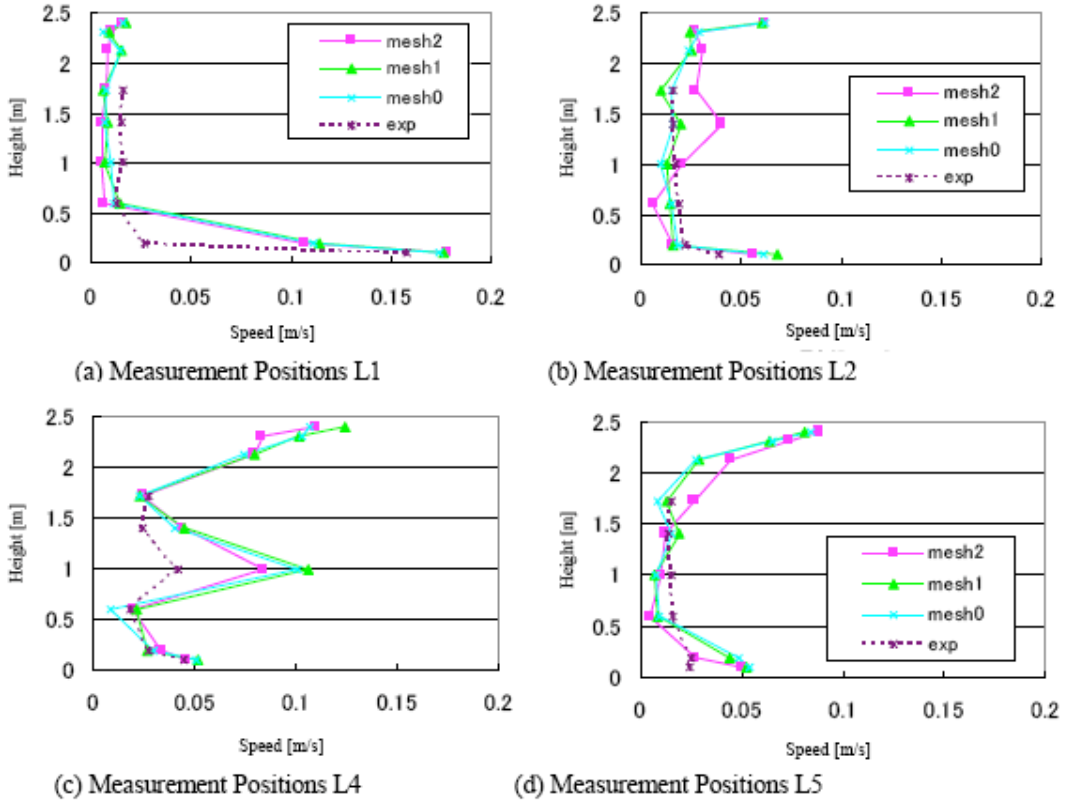

Figure 21: Air speed distributions in the chamber.

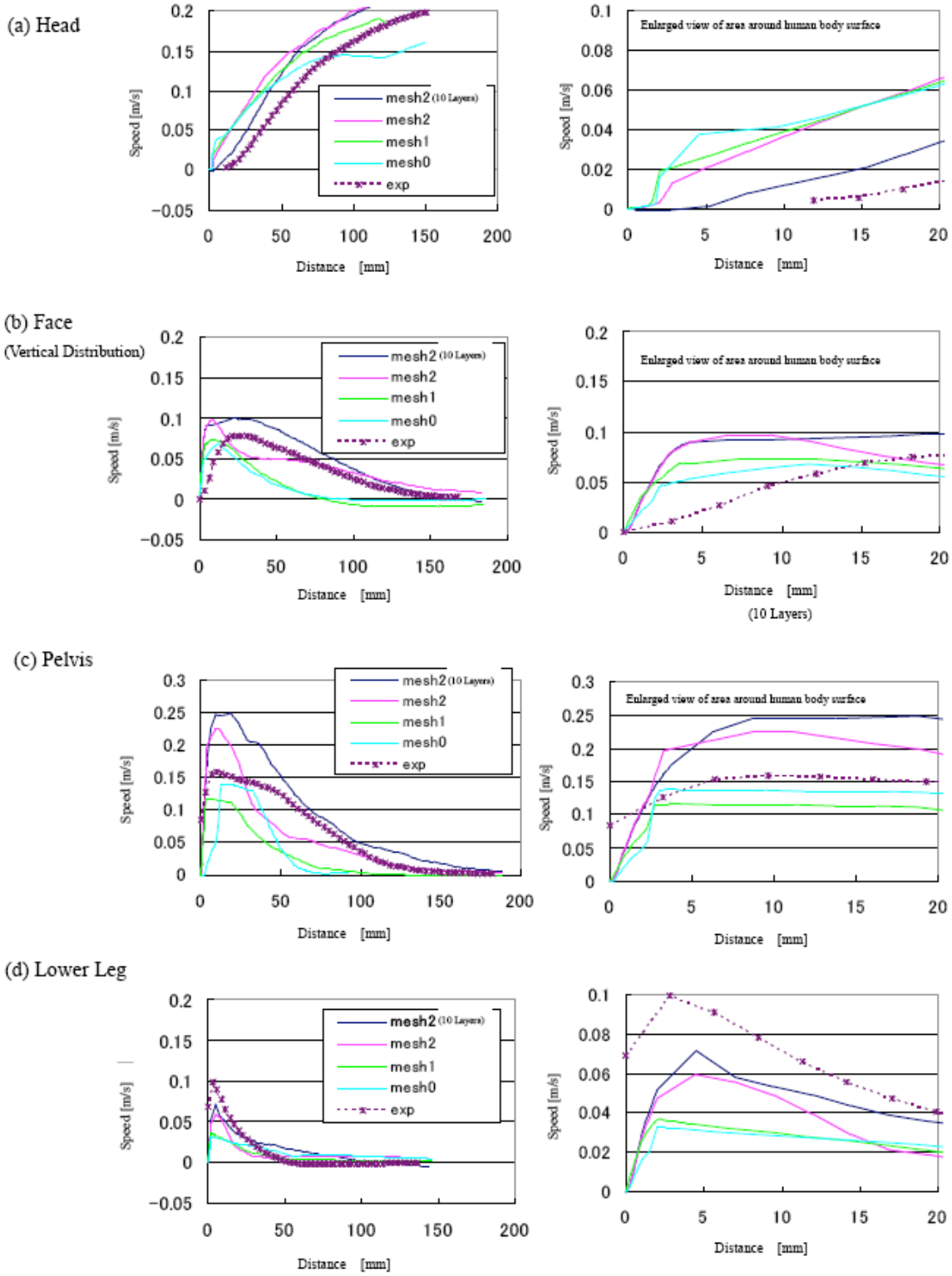

Figure 22: Calculated and measured air velocity distributions around the manikin.

showed sharp increases in front of the manikin starting at just a few millimeters and reaching a maximum speed at 20–30 mm from the manikin surface. Thereafter, air velocities gradually decreased. The maximum velocity was found a few millimeters from the lower leg area, 10 mm from the pelvis, and 20 or 30 mm from the facial surface (20 mm in the measurements). The lower-leg area was near the lower end of the boundary layer that forms around the manikin surface. The maximum air velocity location continued to move outward at the head region, which indicates boundary layer growth. The air velocity

profiles from measurements and simulation generally agreed; however, differences occurred in maximum velocities and its the horizontal location. In the chest and pelvis areas, the calculated maximum velocities and its location were both overestimated compared with the measured values. In the lower leg regions, the measured maximum velocity was close to the manikin, and its locations were generally too large. For upward flows from the top of the head, calculated and measured air velocities were consistent, although distances varied marginally. In the lower leg and head regions, there was a high degree of coincidence between measured values and calculated results using the fine mesh (Mesh2) with 10-layer boundary layers. However, in abdominal and facial regions, Mesh0 and Mesh1 had higher levels of agreement.

Figure **23** shows air temperature distributions inside the chamber. Although calculated values for temperature were about 1°C lower than measured values, the profiles are near consistent. The inlet air temperature was set to 21.8°C following Kato and Yang (n.d.). However, the measured value immediately behind the inlet was 22.8°C (Figure **23a**).

To check this discrepancy, we performed an analysis assuming that the chamber was wall insulated, we estimated the increase in air temperature, Δt, that only resulted due to the heat emitted by the thermal manikin, $Q = \rho C_p V \Delta t$ (where, ρ = density of air, C_p = isobaric specific heat of air, V = air flow rate, and Q = amount of heat emitted by the thermal manikin). Since the thermal manikin did not have any heaters around

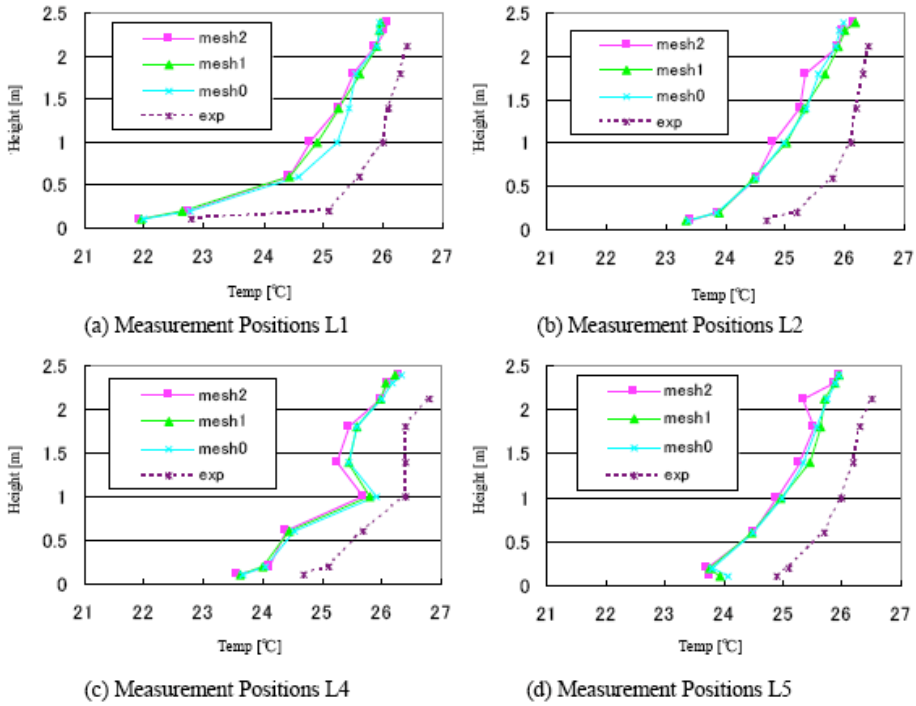

Figure 23: Calculated and measured distributions of air temperatures.

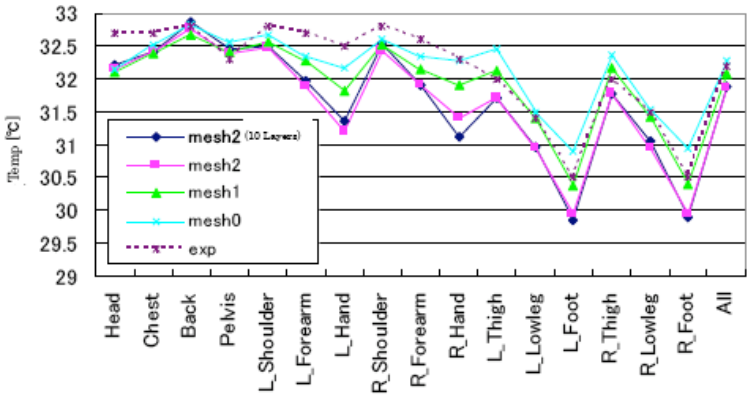

Figure 24: Comparison between temperatures at each region of the manikin.

the leg regions, we set the area of the heated surface to 1.4 m^2. Then, 1.197 × 1007× (0.4 × 0.2 × 0.182) Δt = 51.6 × 1.4 = 72.2 W, hence, Δt = 4.1°C. Therefore, if the inflow air temperature was 21.8°C, then the outflow air temperature would be 25.9°C. In the same way, if the inflow air temperature was 22.8°C, then the outflow air temperature would be 26.9°C. The measured temperature for the upper area of L5 near the flow outlet was 26.5°C. This analysis suggests that it is likely that the inlet temperature was 22.8°C.

Figure **24** compares measured and calculated values for temperatures at each region of the manikin. The difference between measured and calculated temperatures of the hand and front of arms from Mesh2 (fine) were about 0.7–1°C, whereas differences for the head, lower legs, and feet were about 0.5°C. Overall, the calculated temperatures were slightly underestimated compared with the experimental results. No significant differences occurred between boundary-layer cell numbers of five and ten. Manikin surface temperatures from Mesh1 and Mesh0 were generally in better agreement with measured values than the calculated results from Mesh2.

Since the heat flux was constant in this study, if the indoor temperature, t_o, falls, then according to the expression $q = h_t (t_{sk} - t_o)$ = constant, the temperature of the manikin surface, t_{sk}, must also fall. As shown in Figure **23**, we think that this may result from the calculated indoor air temperature being about 1°C less than the measured value.

Figure **25** shows the temperature distribution over the surface of the manikin. Calculated results using the boundary-layer cell number 10 showed slightly higher temperatures around the top of the head and lower temperatures around the thighs compared with those obtained using boundary-layer cell number 5. Temperatures for the top of the head are a little lower, and temperatures of the thighs and lower legs are slightly higher for mesh1 compared with mesh2. In

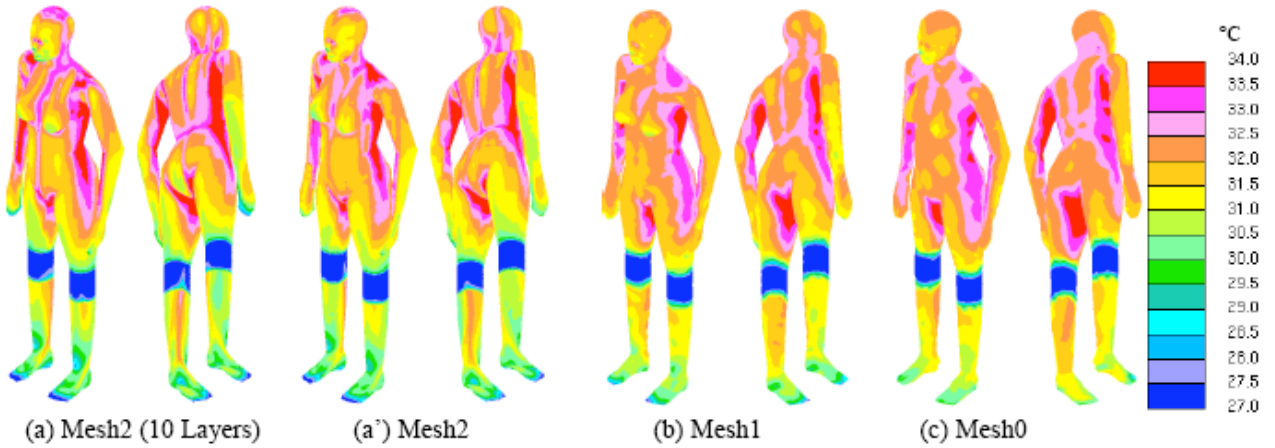

Figure 25: Temperature distributions over the manikin surface.

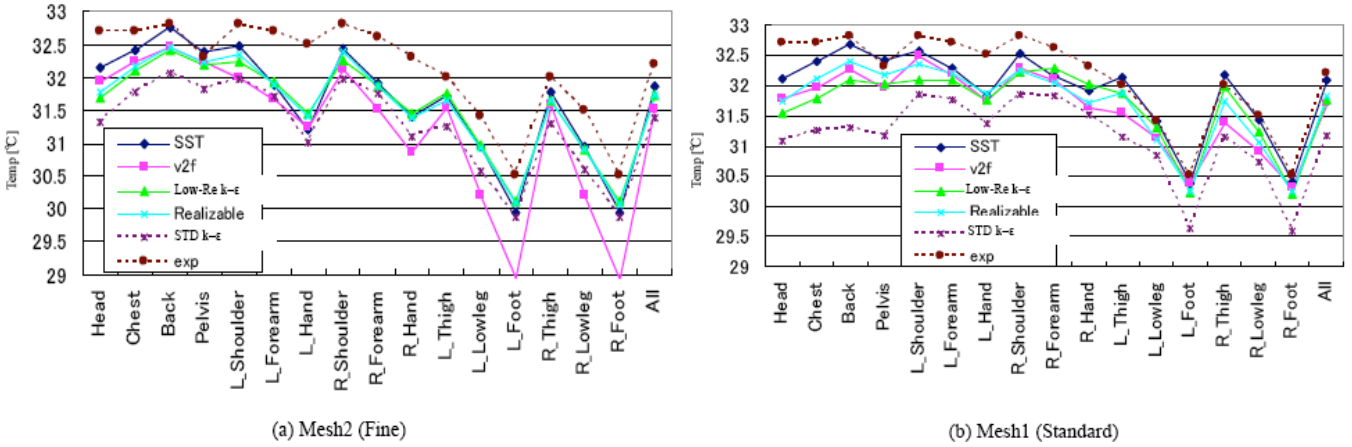

Figure 26: Temperatures over the manikin calculated using different turbulence models.

general, as the mesh resolution increases (so the number of layers in the boundary-layer cell increases), we obtain increasing resolution in the temperature distributions over the manikin surface, and surface temperatures start to average out.

Figure **26**(**a**) shows the surface temperatures of the manikin computed using Mesh2 for the different turbulence models. The calculated results for surface temperatures of the manikin are comparatively close to measured values, regardless of which turbulence model was used. The reasons for this have been discussed in the previous section. Of all turbulence models used, the SST k-ω model provided values that were relatively close to the measurements. The results using the realizable k–ε model were almost the same as those from the low-Re k–ε model. Temperatures around the feet, lower legs, and hands were underestimated by the v2f turbulence model. Compared with other models, results for upper body regions were slightly lower using the high-Re k–ε model.

Figure **26**(**b**) shows calculated results using Mesh1. The temperature of the upper body for Mesh1 was higher than Mesh2 when using the SST k-ω model, and was nearly consistent with measured temperatures. The temperatures of hands and front chest were also higher and approached measured values. When the high-Re k–ε turbulence model was used, the temperatures from Mesh1 were generally less than those from Mesh2, and they tended to move away from experimental values. These trends from the SST k-ω model were also observed when other models were used.

Based on results in Figure **26**, the coarse mesh may seem to be in good agreement with measured values; however, the calculated value of the air temperature was 1°C less than the measured value. If we consider the expression $q = h_t (t_{sk} - t_o)$ = constant and correct t_o by raising it by 1°C, then the surface temperature of the manikin will also increase by 1°C; consequently, calculated values from Mesh2 will move closer to experimental values. As discussed earlier, there is a high possibility that the inflow air temperature was 22.8°C instead of 21.8°C. The latter value was the preset temperature in this analysis. Therefore, to verify the results, an analysis needs to be performed using a preset temperature of 22.8°C.

We evaluated differences that were attributable to using alternative difference schemes. Figure **27**(**a**) shows calculated surface temperatures of the manikin when Mesh2 was used with the MARS or UD (a first order upwind) difference schemes. The UD method generally underestimated manikin surface temperatures by about 0.6°C compared with MARS. Figure **27**(**b**) shows calculated results in which Mesh1 was used. The calculated values from UD increased a little and moved closer to the measured values but results from MARS were still better. It is apparent that the difference scheme affects the calculated results, which is why we tried to avoid using the first-order upwind scheme whenever possible. Generally, we should use upwind difference schemes of second-order or above.

Kato and Yang (n.d.) have performed this test, except they performed an unsteady (transient) analyses using non-linear Re k–ε models, MARS as the difference scheme, and PISO as the pressure-velocity coupling. The mesh consisted of 34,000 elements on the surface walls, and 600,000 elements in the fluid domain. The calculated results for air velocity distributions, temperature distributions, and manikin surface temperatures nearly matched the experimental results.

2.3. Thermal Manikin in a Wind Tunnel with Relatively Strong Wind

2.3.1. Analysis Target Model

A thermal manikin (body height = 1.67 m, surface area = 1.47 m^2) in the Figure of a woman was placed in an upright position inside a wind tunnel. The tunnel dimensions were width = 1.8 m, height = 1.8 m, and length = 17.0 m. The thermal manikin was suspended from the ceiling about 5 cm above the floor, and the surface temperature was controlled to be constant at 33.7°C. An insulation board was placed 0.2 m away from sidewalls of the wind tunnel, and the temperature in the wind tunnel was controlled and constant. This experiment was performed by Ono *et al*. [9,10] at the Institute of Industrial Science, University of Tokyo. Three different inlet air velocities: 0.5, 1.0, and 2.0 m/s were evaluated. Table **5** summarizes the experimental conditions and setup values. Turbulence intensity was measured at the manikin location after removing the manikin. Wall surfaces were assigned identification numbers, as in Figure **28**.

Figure **29** shows a schematic of the setup. A uniform airflow entered the tunnel *via* the inlet in front of the manikin, at a temperature between 30.0°C and 30.2°C and the three cases studied were: Case1, Case2, and Case3 at inlet air velocities of 0.5, 1.0, and 2.0 m/s, respectively.

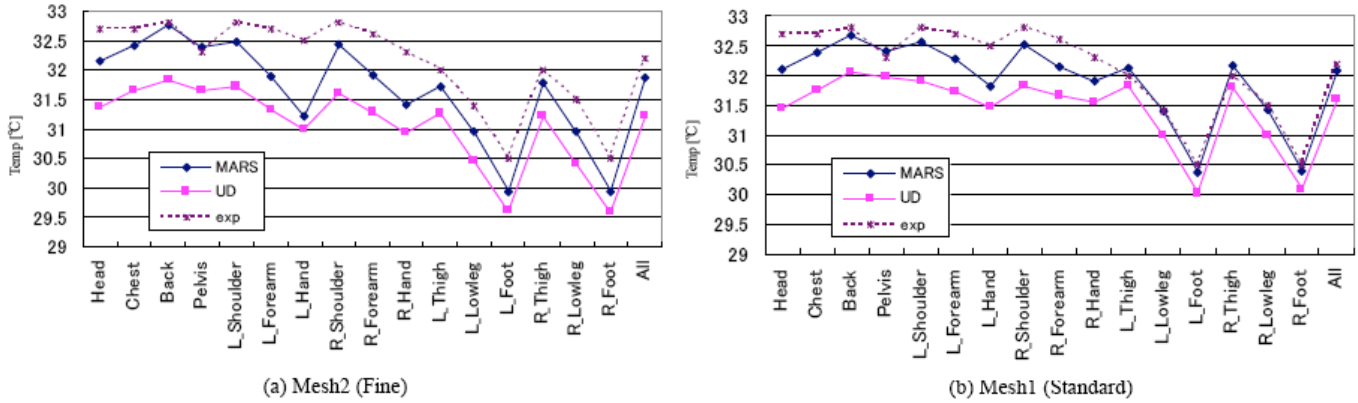

Figure 27: Manikin surface temperatures calculated using the MARS and 1st-order UD difference schemes.

Table 5: Values Measured for Each of Three Experimental

Case	Inflow Temp [m/s]	Turbulence Intensity [%]	Influx Temp [°C]	Peripheral Wall Temp [°C]					
				①	②	③	④	⑤	⑥
Case 1	0.5	11.2	30.1	27.3	28.0	27.3	27.9	26.0	27.3
Case 2	1.0	11.6	30.0	28.1	28.5	28.5	28.4	27.3	28.1
Case 3	2.0	11.9	30.2	28.7	29.1	28.8	29.3	28.0	28.7

Figure 28: Identification numbers for peripheral walls.

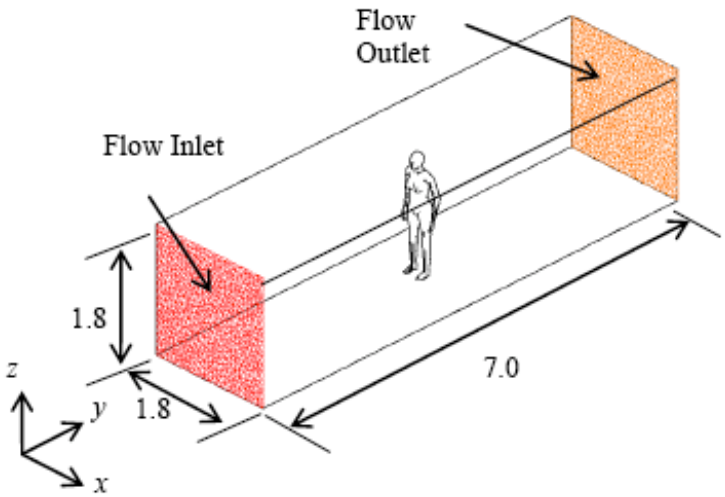

Figure 29: Schematic of wind tunnel.

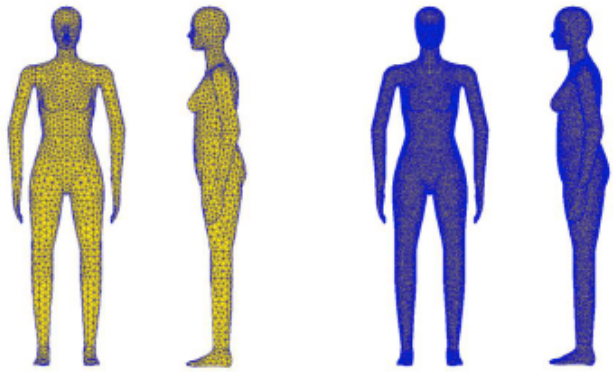

(a) Mesh1 (normal mesh) (b) Mesh2 (fine mesh)

Figure 30: Mesh partition states on the manikin surface.

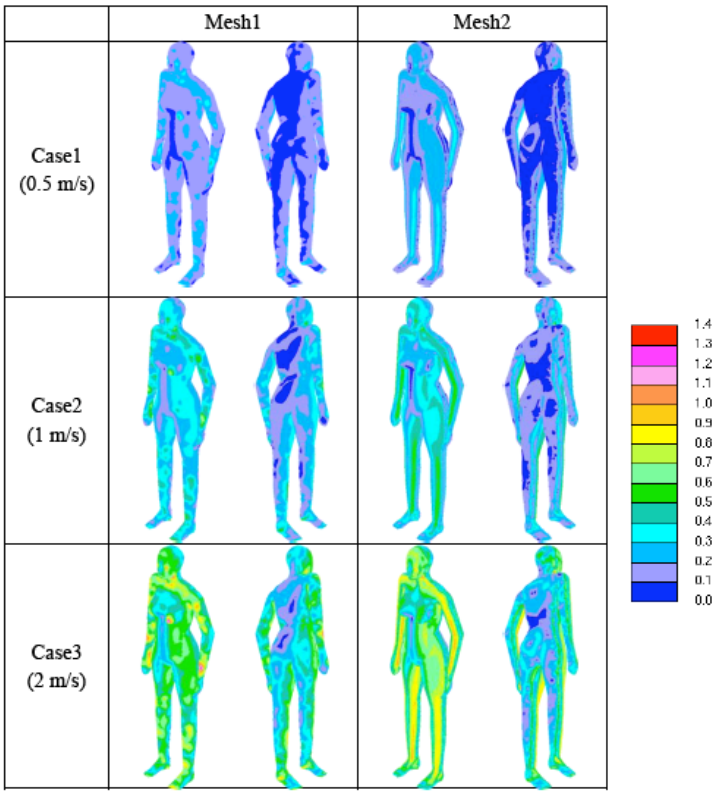

Figure 31: Distribution of *y+* values on the manikin surface.

2.3.2. Analysis Outline

In the CFD setup, inlet boundary conditions for air temperature, velocity, wall surface temperature, and turbulence intensity were applied based on Table **5** data. Skin surface temperature of Manikin was set constant at 33.7°C (knees were insulated), Emissivity of manikin surface and surrounding wall surface were set at 0.95 and 0.94 respectively. For turbulence, the SST k-ω turbulence model was used and, MARS is adopted for discretization scheme. For radiation analysis, CalcRad (Monte Carlo method + Zone method) was used [7].

To determine mesh independence, two mesh designs were created; one, a standard mesh with 580,000 elements, and a fine mesh with 1,660,000 elements. In Mesh1, the thicknesses of the wall-surface first cell prism boundary-layer mesh were 0.1 mm for the manikin and 0.2 mm for the wind tunnel. In Mesh 2, the values were 0.18 mm for the manikin and 0.36 mm for the tunnel. The enlargement ratios for the cell thickness of the boundary-layer mesh were 1.1 for the manikin and 1.3 for the tunnel. The number of layers was set to five in all cases. Figure **30** shows the mesh partitioning, and Figure **31** shows the distribution of y^+

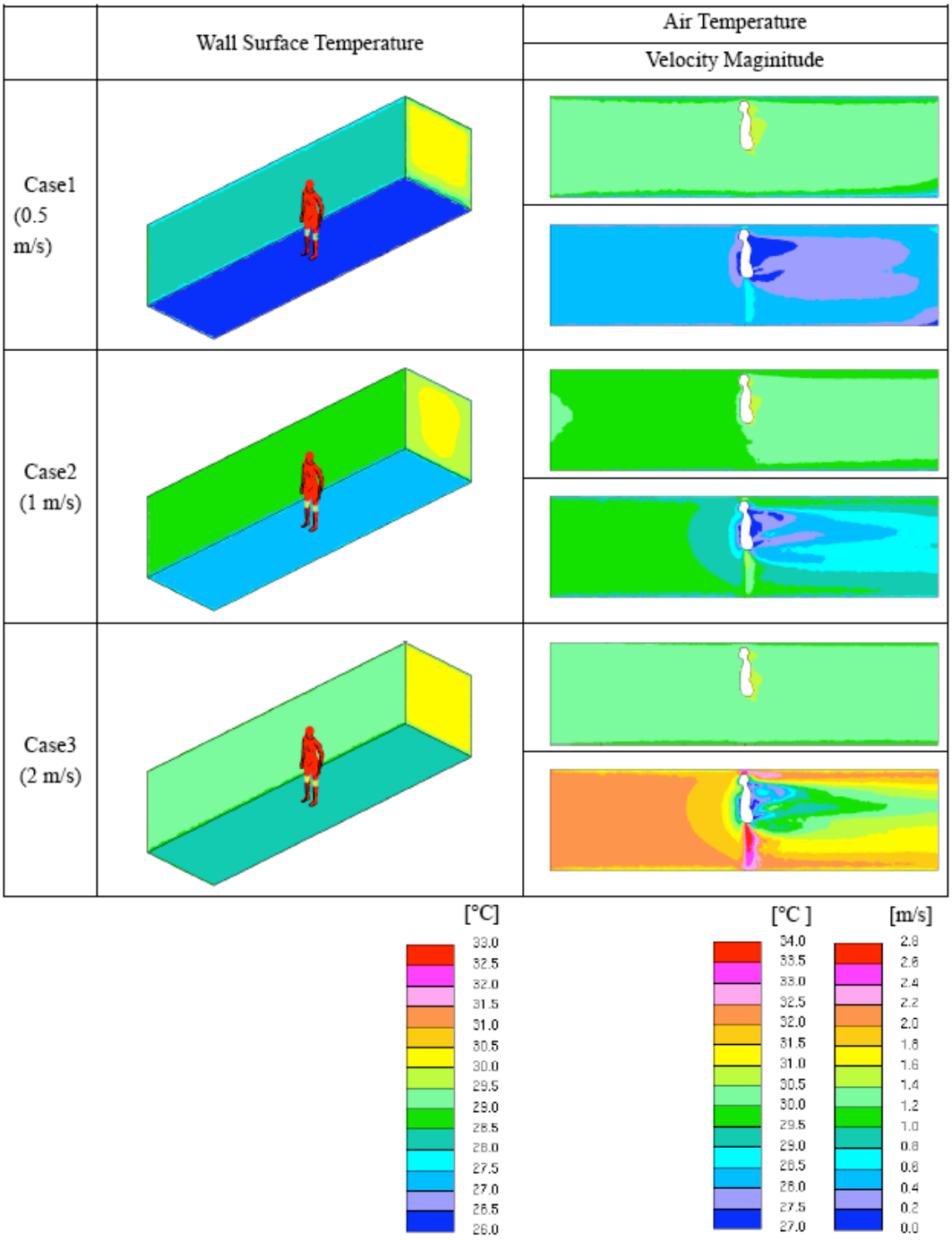

Figure 32: Distributions of wall-surface temperatures, air temperatures, and velocity magnitudes for the three experimental cases.

values on the manikin surface. Values for y^+ increase as the inflow speed increases; but even in Case 3, where the inflow speed was largest (2 m/s), values for y^+ remained less than one.

2.3.3. Analysis Results

Figure **32** shows distributions of wall-surface temperatures, air temperatures, and air velocity for the three cases.

Figure **33** shows the measured and calculated values of convective heat flux (q_c), radiative heat flux (q_r), and total heat flux (q_c + q_r) for an inlet velocity of 0.5 m/s (Case 1). The total heat flux was measured, and we determined values for radiative and convective flux by calculating the radiant heat transfer from measured surface temperatures on the peripheral walls. Consequently, the experimental values for radiative heat flux were actually estimated by numerical

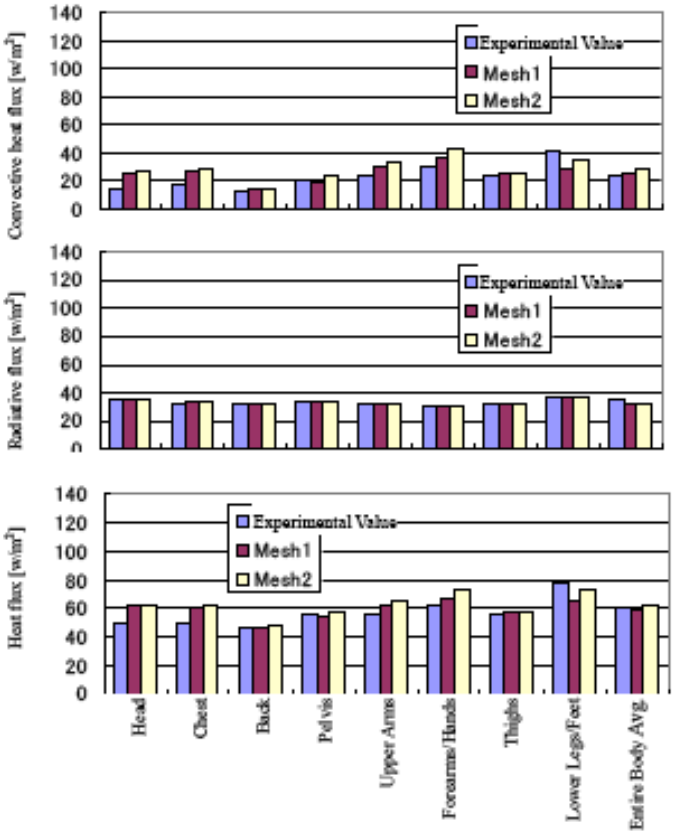

Figure 33: Calculated and measured values for heat flux for each region of the manikin in Case1 (0.5 m/s).

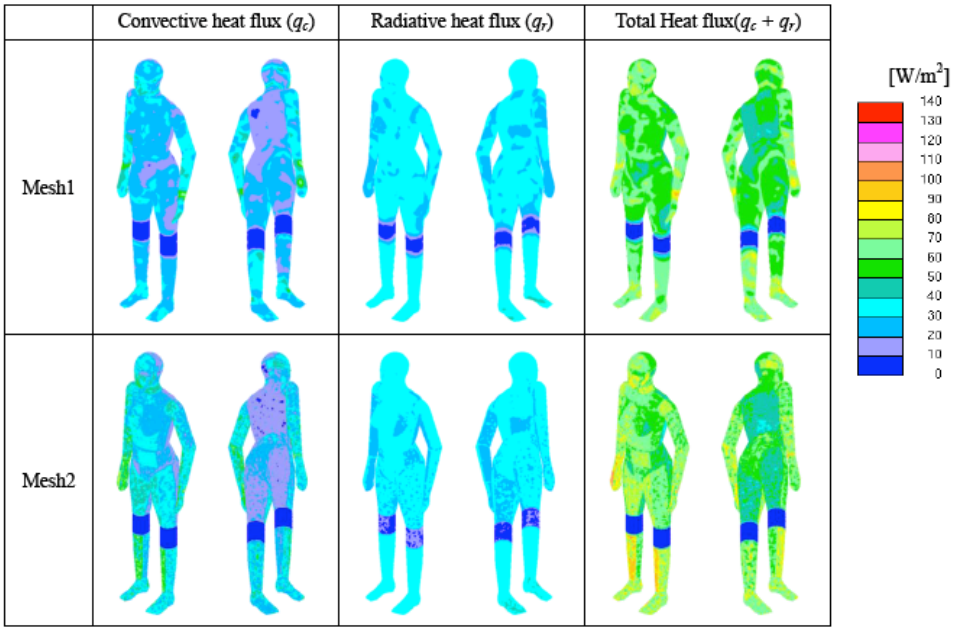

Figure 34: Calculated heat flux distributions over the manikin surface for Case1 (0.5 m/s) and two meshes.

simulation. We then obtained the convective heat flux by subtracting the radiative heat flux from the total.

Measured values in wind tunnel experiment were larger than calculated values for the head, chest, upper arms, and hands but smaller for the lower legs and feet. However, calculated averages over the whole body agreed very well with experimental results.

Calculated heat flux distributions over the manikin surface are shown in Figure **34**. Results from Mesh2 were higher than from Mesh1, particularly for the

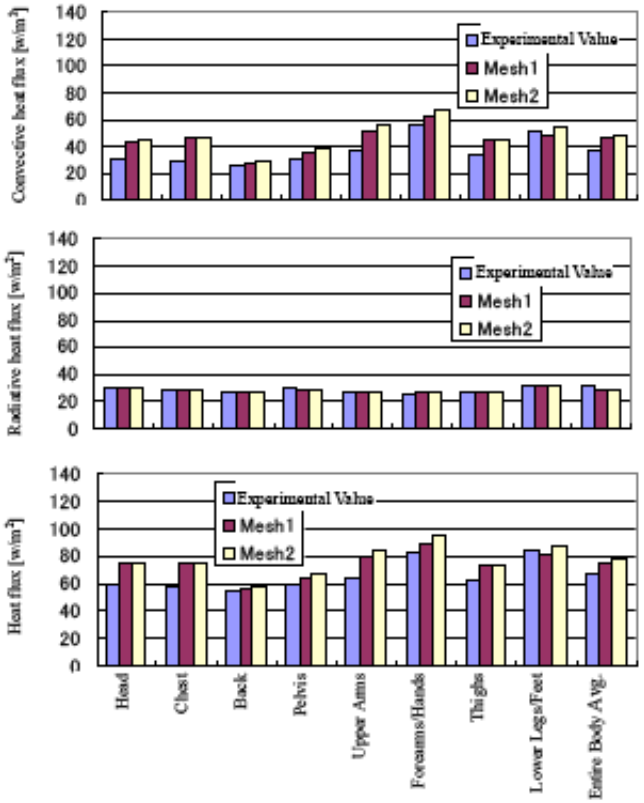

Figure 35: Calculated and measured values for heat flux for each region of the manikin in Case2 (1 m/s).

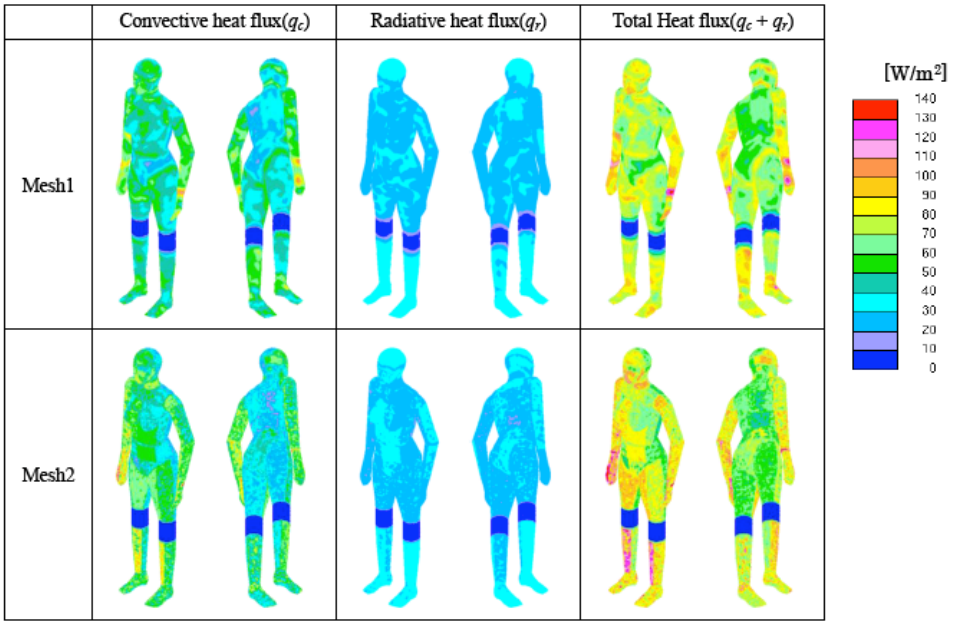

Figure 36: Calculated heat flux distributions over the manikin surface in Case2 (1 m/s).

forearms, hands, thighs, lower legs, and feet, suggesting higher localized heat fluxes.

Figure **35** shows calculated and measured values for convective heat flux (q_c), radiative heat flux(q_r), and total heat flux (q_c + q_r) for an inlet velocity of 1 m/s (Case 2). Although the calculated values for back, lower legs, and feet almost match the measured values, all calculated values for other body regions are too large. The calculated values for averages over the whole body are also relatively larger than measured values. The convective heat flux is slightly overestimated by Mesh2 compared to Mesh1.

Figure **36** shows the heat flux distribution over the manikin surface. Results calculated with Mesh2 are higher than those with Mesh1, particularly for the mouth, forearm, hands, thighs, and lower legs. These results indicate that the local heat flux is large in Mesh2 for each of these body regions.

Figure **37** shows calculated and measured values of convective heat flux (q_c), radiative heat flux (q_r), and total heat flux ($q_c + q_r$) for an inflow air speed of 2 m/s (Case 3). Calculated values are larger than experimental values for all body regions. The convective heat flux is slightly overestimated by Mesh2 compared with Mesh.

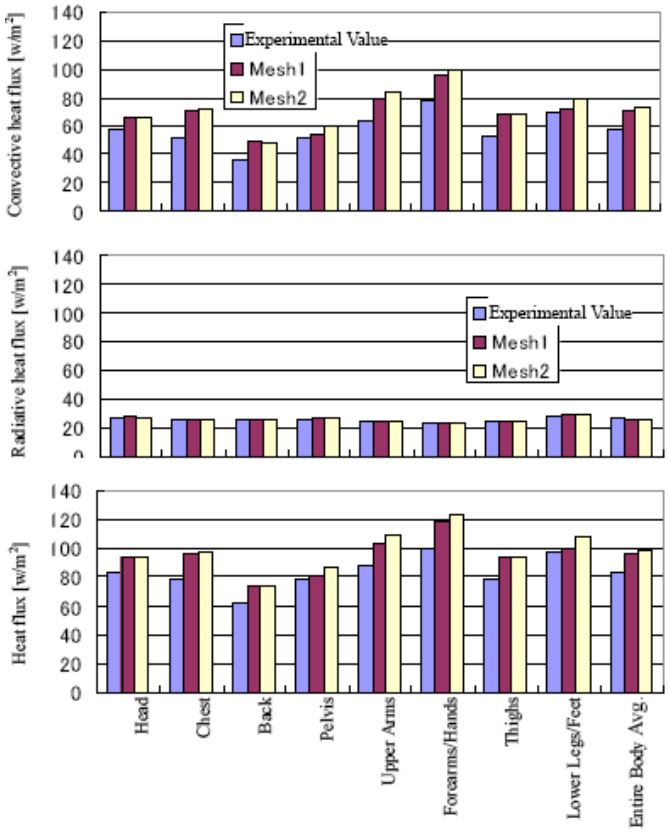

Figure 37: Calculated and measured values for heat flux for each region of the manikin in Case3 (2 m/s).

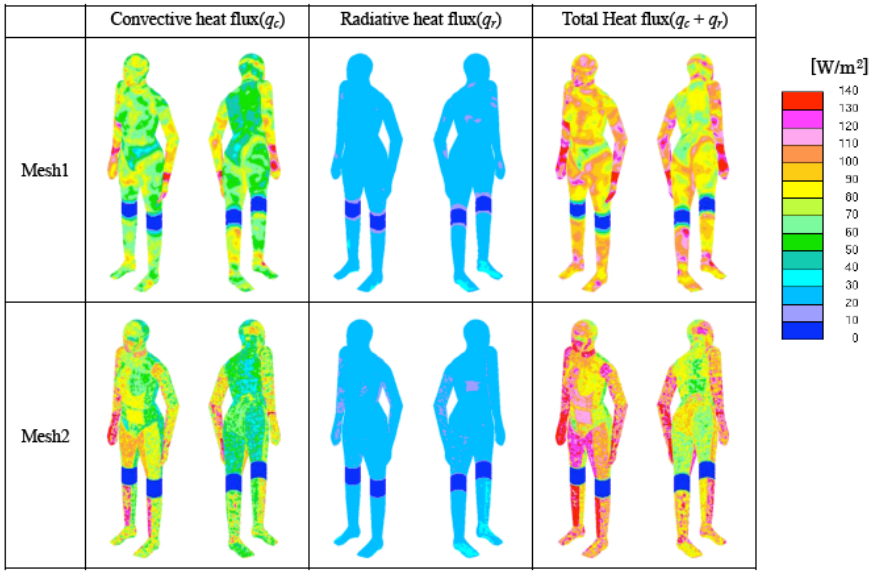

Figure 38: Calculated heat flux distributions over the manikin surface in Case3 (2 m/s).

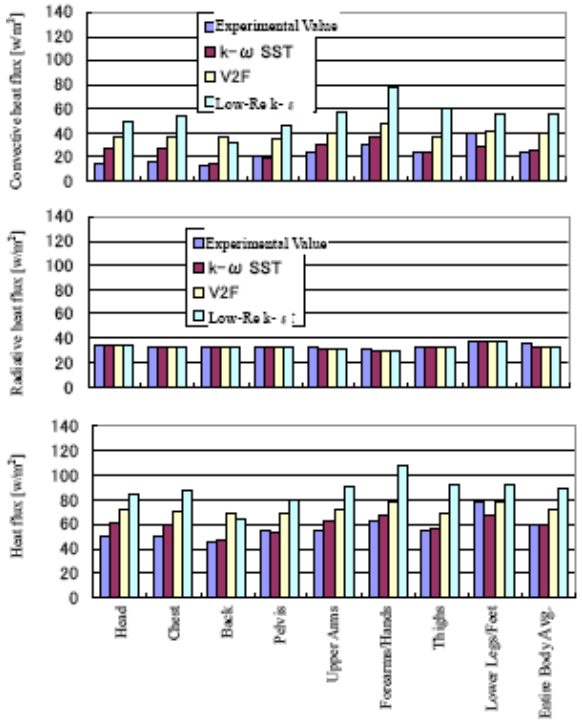

Figure 39: Effects of turbulence model on calculated values of heat flux for each body region.

Figure **38** shows the heat flux distribution over the manikin surface. Results calculated with Mesh2 are higher than those with Mesh1, particularly for the face, forearm, hands, thighs, lower legs and feet.

2.3.4. Discussion

To verify differences caused by using different turbulence models, we performed calculations using the SST k-ω, v2f, and Low-Re k–ε model. The results were obtained for Case1 (U_{in}=0.5 m/s) and Mesh1 were used. The convective heat flux computed from the SST k-ω model discussed earlier closely matched measured values. Figure **39** shows that the v2f model overestimates the convective heat flux, while the low-Re k–ε model produced twice the experimental values; although the margin of error was large.

For this we used the SST k-ω turbulence model and a high-Re k–ε turbulence model (standard k-ε model). We begin with Mesh2 for the grid design of the manikin and the wind tunnel, and set the thickness of the first cell of the wall surface to 20 mm for the manikin and the tunnel, and set the number of layers to one. Figure **40** shows the calculated and measured values for the convective heat flux and the distribution of y^+ values on the surface of the manikin. In Case 1 (0.5 m/s) with the high-Re k–ε turbulence model, the value of *y*+ was

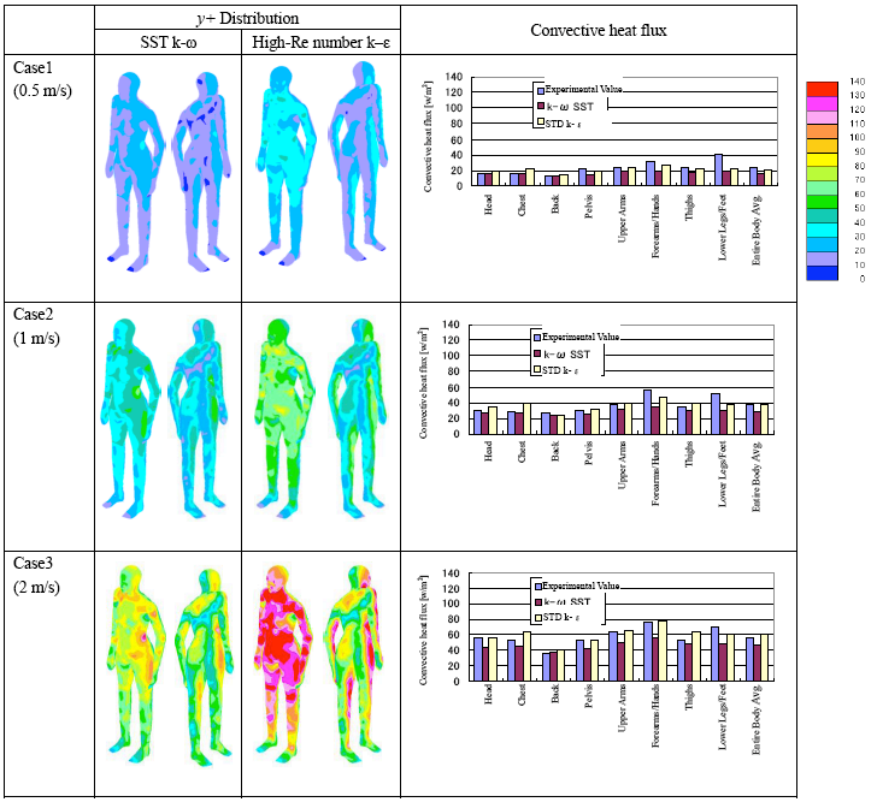

Figure 40: Surface distributions of *y*+ (left) and comparisons between measured and calculated values for convective heat flux (right).

about 7 at the toes and about 10–30 for the feet and back. We found that these *y*+ values were too small to be used in the wall function. For Case2 (1.0 m/s) *y*+ was about 30, and for Case3 (2.0 m/s) *y*+ was over 30 with a maximum of 180.

In Case 1 (0.5 m/s), the SST k-ω model gave calculated values close to experimental values for the upper body, but calculated values for other body regions were lower than measured values. In contrast, values calculated with the high-Re (standard) k–ε model almost matched the measured values for all body regions except the lower legs and feet, where they were smaller. Similar trends were observed in Case2, and in Case3. Generally, the calculated values from the high-Re k–ε model agreed well with the measurements. In these cases, we were able to calculate the convective heat flux with high accuracy using the high-Re (standard) k–ε model. This was accomplished by creating a mesh and making it fall into the applicable range (y^+ = 30–500) for the wall function, (there were instances of y^+ being less than 30 in Case1). However, when using other CFD software, there is no guarantee that we can obtain results with the same high level of accuracy, highlighting the importance of performing validation.

Figure **40** Surface distributions of y^+ (left) and comparisons between measured and calculated values for convective heat flux (right).

To control the overproduction of turbulence kinetic energy, *k*, due to the impinging air stream, Ono *et al*. [9,10] used the Lien–Chen–Leschziner third-order non-linear Re k–ε model, together with an improved version of the Launder–Kato model to evaluate the production term. They then used a corrected turbulence model in performing the analysis. The mesh contained 13,042 elements for the surface walls (manikin model = 5,612/13,042), and 350,000 for the fluid domain.

Figure **41** shows the measured and calculated values from Ono *et al*. [9,10] for the convective heat flux compared with the SST k-ω model in this study for three different inlet velocities (0.5, 1, and 2 m/s). The results showed that convective heat flux was over-predicted at the head, lower legs, and feet. In the chest region, measured and calculated values matched. Therefore, if we exclude these items from comparison, there are no large differences in values calculated using the SST k-ω model.

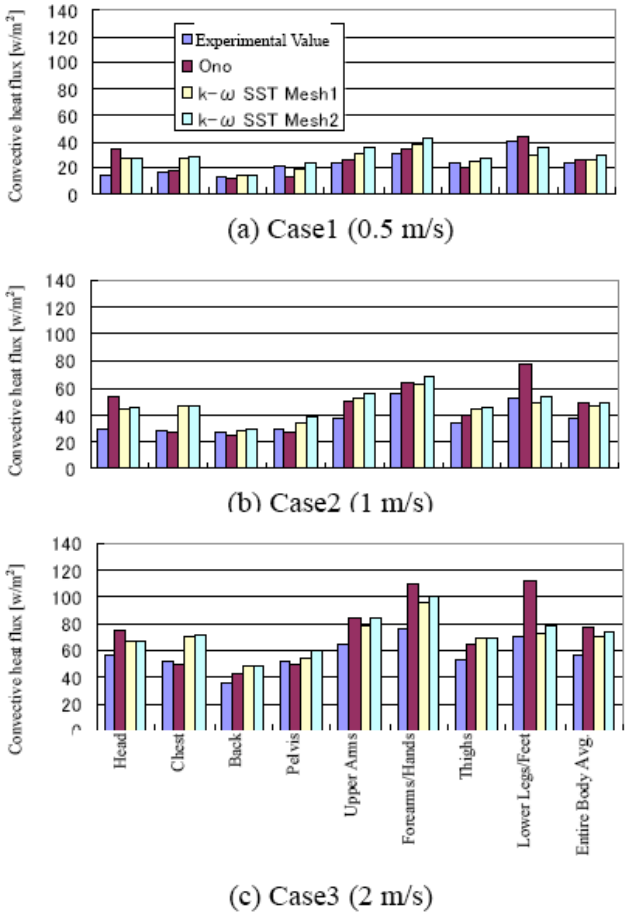

Figure 41: Comparisons of convective heat flux at selected regions on the manikin.

3. CONCLUSIONS

In this paper, benchmark test results for numerical thermal manikins, were discussed. The application of numerical thermal manikin in enclosed space has increased attention recently and there is a need to ensure prediction accuracy in the simulations. The manikin has been applied to special and extreme environmental conditions in addition to a general indoor environment. For example, Li and Ito [11] reported numerical simulation for targeting industrial air-shower systems that included a thermal manikin to reveal fundamental designs for industrial applications. Ito [12] (2014) also reported the integrated simulation procedure from building scale to respiratory tract by way of numerical thermal manikin for precise respiratory exposure analysis. The technique of numerical thermal manikin is also applicable to outdoor environment. Li and Ito [11,13] reported the skin surface distribution of convective heat transfer coefficients on human body under strong wind (from 1 m/s to 20 m/s), and also discussed prediction accuracy by using experimental data in wind tunnel experiment.

The application field of the numerical thermal manikin will widely expand not only thermal sensation analysis in indoor environment but also health impact analysis including respiratory exposure analysis. Numerical thermal manikin technique will contribute to the demand for more sophisticated indoor environmental design against the background of the recent development of computer performance.

NOTE

CFD software in conducting benchmark tests were as follows;

(1) Code A: ANSYS/FLUENT®

(2) Code B: ANSYS/CFX®

(3) Code C: CRADLE/STREAM®

(4) Code D: IDAJ/STAR-CD®

(5) Code E: CRADLE/SCRYU Tetra®

(6) Code F: IDAJ/ STAR-CCM+®

(7) Code G: Open FOAM®

(8) Code H: Advanced Knowledge Laboratory/ Flow Designer®

REFERENCES

[1] Ito K, Inthavong K, Kurabuchi T, Ueda T, Endo T, Omori T, *et al*. Benchmark Tests Associated with Applying CFD to Indoor Environmental Problems: Part 1 Benchmark test for isothermal/non-isothermal flow in 2D and 3D room model. Int J Archit Eng Technol. 2015; 2(1): 50-71

[2] Ito K, Inthavong K, Kurabuchi T, Ueda T, Endo T, Omori T, *et al*. Benchmark Tests Associated with Applying CFD to Indoor Environmental Problems: Part 2 Benchmark test for cross-ventilation airflows and floor heating systems. Int J Archit Eng Technol. 2015; 2(1): 72-98.

[3] ISO-14505-2. Ergonomics of the thermal environment - Evaluation of thermal environments in vehicles, Part 2 Determination of equivalent temperature. 2006.

[4] Nielsen PV, Murakami S, Kato S, Topp C, Yang JH. Benchmark Tests for a Computer Simulated Person, 2003; ISSN 1395-7953 R0307.

[5] Martinho N, Lopes A, Silva N. CFD Modeling of Benchmark Tests for Flow around a Detailed Computer Simulated Person, in 7th International Thermal Manikin and Modeling Meeting. 2008.

[6] Håkan O, Nilsson HB, Nielsen PV. Benchmark Tests of Thermal manikin on a chair in direct contact with countercurrent airflow: www.cfd-benchmarks.com [27 December 2014].

[7] Omori T, Yang J, Kato S, Murakami S. Radiative Heat Transfer Analysis Method for Coupled Simulation of Convection and Radiation in Large-Scale and Complicated Enclosures: Part 1-Accurate Radiative Heat Transfer Analysis based on Monte Carlo Method. Trans Soc Heat Air-cond Sanit Eng Japan, 2003; 88:103-113.

[8] Kato S, Yang J. Benchmark Tests of CFD of Airflow around Human Body in a Room with Displacement Ventilation: www.cfd-benchmarks.com [6 June 2013].

[9] Ono T, Murakami S, Ooka R, Omori T. Numerical and experimental study on convective heat transfer of the human body in the outdoor environment. J Wind Eng Industrial Aerodyn. 2008; 96: 1719-1732. http://dx.doi.org/10.1016/j.jweia.2008.02.007

[10] Ono T, Murakami S, Ooka R, Takahashi T, Omori T, Saotome T. Evaluation Of Mean Convective Heat Transfer Coefficient Of A Human Body In Outdoor Environment: Proposal of the formula for mean convective heat transfer coefficient of a human body by means of wind tunnel and CFD analysis. J Environ Eng AIJ. 2006; 601: 9-14.

[11] Li C, Ito K. Performance Evaluation of Industrial Air-shower System in Removal of Gas- and Liquid-phase Contaminants from Human Body. Evergreen - Joint Journal of Novel Carbon Resource Sciences & Green Asia Strategy 2014; 1: 40- 47.

[12] Ito K. Integrated Numerical Approach of CFD and Epidemiological Model for Multi-scale Transmission Analysis in Indoor Spaces. Indoor Built Environ. 2014; 23: 1029-1049. http://dx.doi.org/10.1177/1420326X13516658

[13] Li C, Ito K. Numerical analysis of convective heat and mass transfer around human body under strong wind. Int J High-Rise Build. 2012; 1: 107-116.

Received on 03-12-2014 Accepted on 18-12-2014 Published on 07-04-2015

DOI: http://dx.doi.org/10.15377/2409-9821.2015.02.01.3